Dear Editor,

We have incorporated the minor revisions in this version by removing the weblinks, citing the data
releases, and adding them to the bibliography section.

Sincerely,
Tarandeep

1

1.1 <u>Marked up manuscript</u>

Development of a Submerged Aquatic Vegetation Growth Model in a Coupled Wave-Current-Sediment Model (COAWST v3.4)

Tarandeep S. Kalra[1], Neil K. Ganju[2], and Jeremy M. Testa[3]

[1]Integrated Statistics, contracted to the U.S. Geological Survey, Woods Hole, MA 02543, USA
[2]U.S. Geological Survey, Woods Hole, MA 02543, USA
[3] University of Maryland Center for Environmental Science, Solomons, MD, 20688, USA

Correspondence to: Tarandeep S. Kalra (tkalra@contractor.usgs.gov)

0 Abstract

The coupled biophysical interactions between submerged aquatic vegetation (SAV), hydrodynamics (currents and waves), sediment dynamics, and nutrient cycling have long been of interest in estuarine environments. Recent observational studies have addressed feedbacks between SAV meadows and their role in modifying current velocity, sedimentation, and nutrient cycling. To represent these dynamic processes in a numerical model, the presence of SAV and its effect on hydrodynamics (currents and waves) and sediment dynamics was incorporated into the open source model COAWST. In this study, we extend the COAWST modelling framework to account for dynamic changes of SAV and associated epiphyte biomass. Modelled SAV biomass is represented as a function of temperature, light, and nutrient availability. The modelled SAV community exchanges nutrients, detritus, dissolved inorganic carbon, and dissolved oxygen with the water-column biogeochemistry model. The dynamic simulation of SAV biomass allows the plants to both respond to and cause changes in water column and sediment bed properties, hydrodynamics, and sediment transport (i.e., a two-way feedback). We demonstrate the behavior of these modelled processes through application to an idealized domain, then apply the model to a eutrophic harbour where SAV dieback is a result of anthropogenic nitrate loading and eutrophication. These cases demonstrate an advance in the deterministic modelling of coupled bio-physical processes and will further our understanding of future ecosystem change.

1 Introduction

Submerged aquatic vegetation (SAV), or seagrasses, are rooted vascular plants that inhabit sediments of estuaries and coastal waters, with a wide global distribution. SAV are important primary producers in shallow environments, provide habitat for a number of aquatic organisms, can slow water velocities and dampen wave energy to trap particulate material (Carr et al., 2004), and can alter biogeochemical cycles through oxygenation of sediments (Larkum et al., 2006). The positive impact of ecosystem services provided by SAV presence has been well-studied

(Hemminga and Duarte, 2000, Nixon et al., 2001, Terrados and Borum, 2004. and McGlathery et al., 2007, Hayn et al., 2014). The growth of SAV is dependent upon light availability at the leaf surface, which is a function of light attenuation in the water-column and the biomass of epiphytic algae growing on SAV stems. During the last several decades, the loss of SAV has accelerated owing to anthropogenic pressures (Kennish et al., 2016) or natural causes such as storms (Hamberg et al., 2017). One of the dominant factors of SAV loss is eutrophication through nutrient loading, exemplified by increased phytoplankton growth and epiphytic growth on vegetation. This results in a reduction of light availability (Burkholder et al., 2007), causing a loss of SAV habitat (Cabello-Pasini et al., 2003, Short and Neckles, 1999).

The complex interactions between light availability, nutrient loading, SAV dynamics, hydrodynamics, and sediment transport can be investigated using numerical modelling tools. Few modelling efforts have attempted to couple the effects of hydrodynamics and light availability to model the growth of SAV. Everett et al., 2007 and Hipsey and Hamilton, 2008 coupled the effects of chlorophyll and water to account for SAV variability while Bissett et al., 1999a, 1999b used spectral underwater irradiance to model the light availability required for SAV growth. Carr et al., 2012a, 2012b developed a one-dimensional coupled hydrodynamics, sediment, and vegetation growth dynamics model. The model solved for vertical 1-D dynamics of SAV growth through a change in biomass that depended on water temperature, irradiance and seagrass properties Ganju et al., 2012 used a three-dimensional circulation model (ROMS) coupled to a Nutrient Phytoplankton Zooplankton Detritus (NPZD) eutrophication (water column bio-geochemistry model) developed by Fennel et al., 2006 and integrated the spectral light attenuation formulation (bio-optical model) provided by Gallegos et al., 2011. These models were linked to a benthic seagrass model to calculate seagrass distribution (Zimmerman et al., 2003) and applied on the temperate estuary of West Falmouth Harbor (del Barrio et al., 2014). While the model was able to capture the loss of SAV due to insufficient light, it did not include interactions with epiphytes or exchanges with water-column nutrient and gas pools. The hydrodynamic feedbacks (change in currents and waves) and morphodynamic changes (sediment distribution) due to presence of SAV were also ignored. While these dynamic processes have significant implications for coastal ecosystem resilience, numerical models that allow for the two-way feedbacks between hydrodynamics, sediment transport, and SAV growth and nutrient cycling have generally been lacking.

Recently, Beudin et al. 2017 implemented the physical effects of SAV in a vertically varying water column through momentum extraction, vertical mixing as well as accounting for wave dissipation due to vegetation. These processes were implemented within the open source COAWST (Coupled-Ocean-Atmospheric-Wave-Sediment Transport) modelling system that couples the hydrodynamic model (ROMS), the wave model (SWAN) and the Community Sediment Transport Modelling System (CSTMS) (Warner et al., 2010). Through this effort, the COAWST framework accounted for the coupled seagrass-hydrodynamics interactions. The model reproduced the turbulent shear stress across the canopy interface and peaked at the top of the canopy similar to the observations of Ghisalberti and Nepf (2004, 2006). The presence of seagrass patch led to a reduced shear-scale turbulence within the canopy and an enhanced wake-scale generated turbulence. For more details on the impact of seagrass on hydrodynamics, readers are referred to Beudin et al. 2017. The inclusion of the physical effects of SAV on flow and sediment dynamics (Beudin

3

et al., 2017) in COAWST allows us to develop a framework that results in dynamic growth of SAV using the temperature, nutrient loading and light availability in the water column. Therefore, in this work we implement a SAV growth model that dynamically changes the SAV properties (stem density and height). The growth of SAV is modeled as biomass which includes the above ground (stems and shoots), below ground (roots and rhizomes) biomass and

5 epiphyte biomass. Individual biomass equations described in the implementation of SAV growth model (section 2.2) are based upon previous SAV biomass models (primarily Madden and Kemp 1996), some of which have been previously implemented to simulate growth conditions for SAV in three-dimensional numerical model simulations (e.g. Cerco and Moore 2001). The change in biomass leads to a spatial and temporal variation of SAV density and height. With the inclusion of the SAV growth model, SAV can grow or dieback while contributing and sequestering

10 nutrients from the water column (modifying the biological environment), and subsequently affect the hydrodynamics and sediment transport (modifying the physical environment). Conversely, a change in the physical environment, for instance the amount of sediment in the water column, can decrease light availability, and cause SAV dieback leading to reduced wave attenuation, increased sediment resuspension, and a further decrease of light availability.

We demonstrate the two-way biophysical coupling framework as follows: the SAV growth model and

15 integration into COAWST are discussed in section 2; in section 3, the model setup for the idealized domain and a realistic simulation of West Falmouth Harbor, MA are described; in section 4, we present the results from the two model configurations along with a discussion of limitations of the current modelling work and in section 5, we summarize our work and outline areas of future research.

20 1 **Methods**

2.1 **Inclusion of SAV effect on flow and sediment dynamics in the numerical model**

Beudin et al. (2017) implemented the parameterizations that accounted for the presence of SAV within a coupled hydrodynamic and wave model within the open-source COAWST numerical modelling system (Warner et al., 2008). The COAWST framework utilizes ROMS (Regional Ocean Modelling System) for hydrodynamics with a

25 wave model - SWAN (Simulating WAves Nearshore) via the Model Coupling Toolkit (MCT) generating a single executable program (Warner et al., 2008). ROMS (Regional Ocean Modelling System) is a three-dimensional, free surface, finite-difference, terrain-following model that solves the Reynolds-Averaged Navier-Stokes equations using the hydrostatic and Boussinesq assumptions (Haidvogel et al., 2008). The transport of turbulent kinetic energy and generic length scale are computed with a generic (GLS) two-equation turbulence model. SWAN (Simulating WAves

30 Nearshore) is a third-generation spectral wave model based on the action balance equation (Booij et al., 1999). In ROMS, the presence of SAV extracts momentum, adds wave-induced streaming, and generates turbulence dissipation. Similarly, the wave dissipation due to vegetation modifies the source term of the action balance equation in SWAN. All these sub-grid scale parameterizations account for changes due to vegetation in the water column extending from the bottom layer to the height of the vegetation. SWAN only accounts for wave dissipation due to vegetation at the

35 bottom layer. The coupling between the two models occurs with an exchange of water level and depth averaged velocities from ROMS to SWAN and wave fields from SWAN to ROMS after a desired number of time steps. The vegetation properties are separately input in the two models at the beginning of the simulations. Through these

4

changes, the SAV can affect the bottom stress calculations that determine the resuspension and transport of sediment, providing a feedback loop between SAV-sediment dynamics-hydrodynamics and wave dynamics. To account for sediment dynamics, the Community Sediment Transport Modelling System (CSTMS) (Warner et al., 2010) is used to track the transport of suspended-sediment and bed load transport under the action of current and wave-current forcing.
5   The model can represent an unlimited number of user defined sediment classes.

2.2 SAV growth model

The SAV growth model is primarily based upon a previous growth model developed and implemented in Chesapeake Bay by Madden and Kemp (1996). The model simulates the temporal dynamics of above ground biomass
10   (AGB) that consists of stems or shoots, and the below ground biomass (BGB) that consists of roots or rhizomes. In addition to AGB and BGB, epiphytic algal biomass (EPB) is simulated to account for reductions in light availability to plant leaves due to shading of SAV leaves by epiphytes under high nutrient loading conditions. AGB, BGB and EPB are simulated as total biomass per unit area, with nitrogen as the currency for biomass. Changes in AGB and BGB pools are simulated as a function of primary production and respiration, mortality (e.g. grazing), and nitrogen
15   exchange through the seasonal translocation of nitrogen between roots and shoots. EPB are modelled as a function of primary production, respiration, and mortality.

The remaining section describes the source terms that calculate the evolution of AGB, BGB and EPB and denoted by α, β and γ respectively. Table 1 and Table 2 describe model variables and input parameters along with their equivalent symbols used in the source code.

20   2.1 Primary production (ρ_s): The primary production of α depends on the maximum potential growth rate (μ_s) and downward deviations from this maximal rate resulting from light (φ_s) and nutrient (ϑ_s) availability as:

$$\rho_s = \mu_s \min(\varphi_s, \vartheta_s) \tag{1}$$

The maximum potential growth (μ_s) can be described as:

$$\mu_s = \lambda_s \vartheta_s g_s \exp[r_s\left(\frac{1.0}{T-T_o}\right)] \tag{2}$$

25   where λ_s is a self-shading parameter that accounts for crowding and self-shading within the SAV canopy, g_s accounts for SAV's maximum growth fraction, r_s is the active SAV respiration coefficient, T is the temperature in water column, T_o is the user defined optimum temperature that allows for species specific sensitivities to temperature. The self-shading parameter, λ_s used in Eq. 3 is calculated by setting a maximum aerial biomass of SAV (Madden and Kemp 1996), thereby making growth rates density-dependent and is defined as:

30   $$\lambda_s = 1 - \left(\frac{\alpha}{\lambda_{s,max}}\right)^2 \tag{3}$$

where α is the above ground SAV biomass and $\lambda_{s,max}$ accounts for the maximal SAV biomass.

The availability of photosynthetically active radiation (PAR) represented by mathematical symbol θ for SAV leaves in the bottom cell is simulated using a bio-optical model (Gallegos et al. 2009, del Barrio et al. 2014). While the bio-

5

optical model generates predictions of light available across the spectrum within PAR, the light availability (φ_s) used to compute primary production (Eq. 1) is obtained through traditional photosynthesis-irradiance (PI) curves based on total PAR used to represent SAV growth responses to light:

$$\varphi_s = \frac{\theta}{l_s + \theta} \tag{4}$$

5   where l_s is the half-saturation for light limitation for SAV and θ refers to photosynthetically available radiation that is obtained from the bio-optical model. This simplified PI formulation, which has been applied in previous SAV models (Madden and Kemp 1996, Zaldívar et al. 2009, Jarvis et al. 2014) is applied so that a general and flexible SAV growth response is available for users in a wide-variety of environments with different species. More complex approaches can easily be applied (e.g. Zharova et al. 2001, Carr et al. 2012). The nutrient limitation (ϑ_s) required in

10   Eq.1 to compute primary production represents the fact that rooted plants can obtain nutrients from both sediments (as in Madden and Kemp, 1996) and the water-column and is defined as:

$$\vartheta_s = DIN_{wc} + \frac{n_{s,1} DIN_{sed}}{n_{s,2} DIN_{sed} + n_{s,1} DIN_{sed}} \tag{5}$$

where DIN_{wc} is the dissolved inorganic nitrogen concentration in the water column based on the sum of NH_4 (Ammonium) and NO_3 (Nitrate) in the water column and DIN_{sed} is the amount of dissolved inorganic nitrogen (DIN

15    $= NH_4 + NO_3$) in the sediment bed layer, and $n_{s,1}$ is the half-saturation for nutrient limitation for SAV roots.

2.2.2 Respiration: SAV respiration terms are partitioned into active and basal respiration, where the active respiration term represents respiration that is dependent on the photosynthesis rate, and the basal rate represents maintenance respiration rate. The active respiration term is defined as:

20    $$\delta_s = \rho_s \, p_s \exp(r_s \, T) \tag{6}$$

where ρ_s is the primary production term (Eq. 1), p_s is the maximum fraction of photosynthesis available for respiration, r_s is the SAV's active respiration coefficient, T is the temperature in the water column. The above ground basal respiration term is defined as:

$$\varepsilon_s = c_s \exp(h_s \, T) \tag{7}$$

25   where c_s is the maximum fraction of SAV below ground biomass (BGB) that is respired, h_s is the SAV basal respiration coefficient for both AGB and BGB, T is the temperature in the water column.

2.2.3 Mortality: The mortality of SAV is computed separately for above-ground and below-ground biomass, where above ground mortality ($\omega_{s,1}$) accounts for the sloughing of leaves and grazing in combination as:

$$\omega_{s,1} = (m_\alpha \, \alpha)^2 \tag{8}$$

30   where m_α is the above ground SAV mortality rate (sloughing).

Below ground mortality, $\omega_{s,2}$, is a function of temperature and is given as:

$$\omega_{s,2} = 0.01 \, \beta \exp(m_\beta \, T) \tag{9}$$

where m_β is the below-ground SAV mortality rate. Additional terms include that modify the AGB and BGB include

35   the seasonal exchange (translocation) of root material (nitrogen) quantified as a fraction of primary production and the translocation of BGB to AGB which represents the seasonal translocation of nitrogen from roots to stems as the

6

plants initially emerge in spring. Each of these terms is initiated on a specified day of the year (Madden and Kemp 1996), and can be altered to account for species differences or regional differences in the physiology of particular species. Translocation of nitrogen from leaves to roots/rhizomes (storage) is modelled as a continuous response to SAV primary production (ρ_s) and is given by defining $\sigma_{s,1}$ (translocation of above ground biomass to below ground biomass) as:

$$\sigma_{s,1} = \rho_s \, k_1 \tag{10}$$

where k_1 is a downward translocation coefficient.

and translocation from roots/rhizomes to leaves (upward translocation) is modelled as a simple linear function of below ground biomass (denoted by β) that begins after a user-defined threshold temperature is crossed and is given by defining $\sigma_{s,2}$ (translocation of below ground biomass to above ground biomass) as:

$$\sigma_{s,2} = \beta \, k_2 \tag{11}$$

where k_2 is a upward translocation coefficient.

The epiphyte biomass (EPB) is computed similarly to SAV biomass by simulating EPB as a function of primary production, respiration, and mortality (e.g. grazing).

2.2.4 Primary production (ρ_e): The primary production of EPB depends on the maximum potential growth rate (μ_e) and a limitation between light (φ_e) and nutrient (ϑ_e) availability, as:

$$\rho_e = \mu_e \, \min(\varphi_e, \vartheta_e) \tag{12}$$

The maximum potential growth of EPB (μ_e) can be described as:

$$\mu_e = \lambda_e \, \vartheta_e \, g_e \, \exp\left[r_e \left(\frac{1.0}{T - T_{e,o}}\right)\right] \tag{13}$$

where λ_e is the self-shading parameter that accounts for spatial limits on the epiphyte population, g_e accounts for epiphyte's maximum growth fraction, r_e is the active epiphyte respiration coefficient, T is the temperature in water column, $T_{e,o}$ is the user defined optimum temperature that allows for species-specific sensitivities to temperature. λ_e is calculated by setting a maximum aerial biomass of EPB, thereby making growth rates density-dependent similar to the SAV growth rate, as:

$$\lambda_e = 1 - \left(\frac{EPB}{\lambda_{e,max}}\right)^2 \tag{14}$$

where EPB is the epiphyte biomass and $\lambda_{e,max}$ is the maximum epiphyte biomass.

The light availability (φ_e) used to compute primary production (Eq. 10) is obtained through traditional photosynthesis-irradiance (PI) curves used to represent epiphyte growth response to light, as:

$$\varphi_e = \frac{\theta}{l_e + \theta} \tag{15}$$

where l_e is the half-saturation for light limitation for epiphytes and θ is the photosynthetically available radiation obtained from the bio-optical model. The nutrient limitation (ϑ_e) required in Eq.1 to compute primary production for

epiphytes depends only on the nutrients in the water-column and is a traditional algal form (e.g. Monod model) given as:

$$\vartheta_e = \frac{n_e \, DIN_{wc}}{n_e \, DIN_{wc} + n_e} \tag{16}$$

where DIN_{wc} is the amount of dissolved inorganic nitrogen in the water column, n_e is the half-saturation for nutrient limitation for epiphytes.

2.2.5 Respiration: Epiphyte respiration terms are partitioned into active and basal respiration, where the active respiration term represents respiration that is dependent on the photosynthesis rate, the basal rate represents the maintenance respiration rate. The active respiration term is defined as:

$$\varepsilon_{e,1} = \rho_e \, p_e \exp(r_e \, T) \tag{17}$$

where ρ_e is the primary production term (Eq. 1), p_e is the maximum fraction of photosynthesis for epiphytes, r_e is the epiphyte's active respiration coefficient, T is the temperature in the water column.

The basal respiration term is defined as:

$$\varepsilon_{e,2} = c_e \exp(h_e \, T) \tag{18}$$

2.2.6 Mortality: The mortality of epiphytes depends on mortality and grazing of algal cells, as well as losses associated with SAV sloughing (which effectively removes epiphytes from a cell). The mortality term is given as a simple linear form:

$$\omega_e = m_e \, \gamma \tag{19}$$

where m_e is the epiphyte mortality rate. The loss of epiphyte biomass due to grazing ($\tau_{e,1}$) modelled using an Ivlev function can be described as:

$$\tau_{e,1} = z_{e,max} \, [1.0 - \exp(-z_e)] \tag{20}$$

where $z_{e,max}$ is the maximum grazing rate on epiphytes and z_e is the grazing coefficient on epiphytes. The reduction of epiphyte biomass due to the SAV sloughing loss is computed as:

$$\tau_{e,2} = \left(\frac{\omega_{s,1} \, t}{\alpha} \right) \tag{21}$$

where $\omega_{s,1}$ is the above ground mortality term described in Eq. 8, is the time step size in per day units and α refers to the above ground biomass.

The above ground biomass (AGB) computed in the SAV growth model is utilized to obtain SAV shoot height (meters) and stem density (stems/m^2), to allow for the biomass model (AGB) to be translated into variables input into the SAV-hydrodynamic coupling. The shoot height (l_v) is related to AGB (denoted by α) as:

$$l_v = 0.45 \left(\frac{\alpha}{120.0 + \alpha} \right) \tag{22}$$

The relationship is based on measurements of *Zostera marina* in Chincoteague Bay and Chesapeake Bay (Fig. 2), but is consistent with relationships for *Z. marina* determined elsewhere (Krause-Jensen et al., 2000). Other three-dimensional models have used similar formulations (e.g. Cerco and Moore, 2001 for Chesapeake Bay). SAV stem

density n_v, (in stems/m^2) is computed from a similar empirical formulation based on relationships in Krause-Jensen et al., 2000 and is computed as:

$$n_v = 4.45\,\alpha \tag{23}$$

2.3 Integration of SAV growth model with Water-Column Biogeochemistry Model (BGCM model)

The SAV growth model is built to interact dynamically with the water-column biogeochemistry model (BGCM model) within the COAWST modelling framework. We utilize one of the existing BGCM models developed by Fennel et al., 2006 that accounts for nutrients (NO_3, NH_4), phytoplankton and zooplankton biomass, and detritus. The BGCM model in the current simulations solved for twelve state variables. The spectral irradiance model that provides the light attenuation in response to chlorophyll, sediment, and CDOM was previously integrated (Gallegos et al. 2009, del Barrio et al. 2014) into the BGCM model. The BGCM model was implemented within the hydrodynamic component of COAWST model, ROMS (Regional Ocean Modeling System). ROMS is a three-dimensional, free surface, terrain-following numerical model that solves finite-difference approximations of the RANS equations using the hydrostatic and Boussinesq assumptions (Chassignet et al., 2000 and Haidvogel et al., 2000). ROMS is discretized in horizontal dimensions with curvilinear orthogonal Arakawa C grid (Arakawa, 1966). Each state variable is calculated based on the tracer transport equation with tracer concentrations calculated at the grid cell centers as follows:

$$\frac{\partial C}{\partial t} + u\frac{\partial C}{\partial x} + v\frac{\partial C}{\partial y} + w_d\frac{\partial C}{\partial z} = \frac{\partial}{\partial z}\left(v\frac{\partial C}{\partial z}\right) + C_{source} \tag{24}$$

where C is the tracer quantity, t is time, x and y are the horizontal coordinates and z is the vertical coordinates. u and v are the horizontal components of current velocity with w_d being the sinking velocity for tracers such as detritus. v is the turbulent diffusivity coefficient and C_{source} is the tracer source/sink term, which represents the net effects of all sources and sinks in this representation. There are several choices of advection schemes for tracer advection available in COAWST (Kalra et al., 2019) and in the current simulations, we utilized Multidimensional Positive Definite Advection Transport Algorithm (MPDATA) scheme (Smolarkiewicz, 1984) that has been derived from Lax Wendroff (LW) family of schemes. The time marching scheme for tracers involves a predictor-corrector step using the leapfrog-trapezoidal methods. The 3-D tracer equations are solved at a different and shorter time step than the depth-integrated 2-D barotropic equations. The integration between the baroclinic mode and barotropic mode is performed using a split-explicit time step approach (Shchepetkin and McWilliams, 2005, 2009). The predictor step calculates the tracer values that updates the momentum equations at an intermediate time step. At that point, the split-explicit algorithm is executed and the update of tracers is done using the corrector step after the new values of velocity are available. For more details of this algorithm, readers are readers are referred to Shchepetkin and McWilliams, 2005 and 2009. The vertical tracer diffusion terms are solved using a fourth-order centered scheme (Shchepetkin and McWilliams, 2005). The vertical advective fluxes are computed using the piecewise parabolic method (Colella and Woodward, 1984). The vertical terms utilize a backwards Euler method for time marching.

The changes in water-column variables (dissolved and particulate nitrogen, dissolved oxygen, dissolved inorganic carbon) due to the SAV growth model occur locally at the bottom cell through the source terms (C_{source}) that affect six state variables in the BGCM model: NO_3 (Nitrate), NH_4 (Ammonium), DO (Dissolved Oxygen), CO_2 (Carbon dioxide), $LDeN$ (Labile Detrital Nitrogen), $LDeC$ (Labile Detrital Carbon). The change in these state variables based on the SAV growth model is as follows:

$$\frac{\partial DIN_{SAV}}{\partial t} = (\delta_s + \varepsilon_s - \rho_s)(1 - s_f)t + (\varepsilon_{e,1} + \varepsilon_{e,2} - \rho_e)t \tag{25}$$

where $\frac{\partial DIN_{SAV}}{\partial t}$ is the net impact of SAV and epiphyte growth on water-column nitrogen concentrations and s_f decides the portioning of nutrient uptake between sediment and water column using a logistic function and is defined as:

$$s_f = 1 - \left(\frac{1}{1+\exp[-m_f(DIN_{wc} - k_f)]}\right) \tag{26}$$

where m_f and k_f are constants and equal to 0.2 and 15.0 respectively and DIN_{wc} (Dissolved Inorganic Nitrogen) is calculated as a sum of state variables NH_4 (Ammonium) and NO_3 (Nitrate) in the water column. If net growth from SAV and epiphytes is negative, the net nitrogen regeneration is realized as NH_4 production in the water column ($\frac{\partial NH_4}{\partial t} = \frac{\partial DIN_{SAV}}{\partial t}$). If there is net growth originating from SAV and epiphytes, the associated water column uptake of DIN is apportioned between NO_3 and NH_4 relative to their availability in the water-column via the following equations:

$$\frac{\partial NH_4}{\partial t} = \left(\frac{\partial DIN_{SAV}}{\partial t}\right)\left(\frac{NH_4}{DIN_{wc}}\right) \tag{27}$$

$$\frac{\partial NO_3}{\partial t} = \left(\frac{\partial DIN_{SAV}}{\partial t}\right)\left(\frac{NO_3}{DIN_{wc}}\right) \tag{28}$$

$$\frac{\partial DO}{\partial t} = \left(\rho_s - \delta_s - \varepsilon_s + \rho_e - \varepsilon_{e,1} - \varepsilon_{e,2}\right)t \tag{29}$$

$$\frac{\partial CO_2}{\partial t} = \left(\delta_s + \varepsilon_s - \rho_s + \varepsilon_{e,1} + \varepsilon_{e,2} - \rho_e\right)t \tag{30}$$

$$\frac{\partial LDeN}{\partial t} = \left(\omega_{s,1} + \omega_e + \tau_{e,1}\right)t \tag{31}$$

$$\frac{\partial LDeC}{\partial t} = \left(\omega_{s,1} + \omega_e + \tau_{e,1}\right)t \tag{32}$$

All the source terms in equations (25 and 27-32) are solved using the SAV growth model described in Section 2.2 and in equation 30 and 32, these terms are converted to moles of Carbon from moles of Nitrogen assuming a fixed (and user-defined based on local data) C:N ratio in SAV tissue (we assumed a C:N of 30).

2.4 Two-way feedback from SAV to hydrodynamics, waves, sediment dynamics, and biogeochemistry

The addition of the SAV growth model leads to the biological evolution of SAV properties based on temperature, light, and nutrient availability. The modelled SAV community exchanges nutrients. detritus, dissolved oxygen, and dissolved inorganic carbon with the water-column BGCM. Changes in SAV biomass, and canopy characteristics also impacts hydrodynamics, wave dynamics and sedimentary dynamics (resuspension-transport). By lowering the current

5 speed and attenuation of wave flow, the reduction in bed shear stresses in the vegetation canopy reduces sediment resuspension; thereby altering sediment transport in the model (as described in Section 2.1), that feedback to control light availability and, in turn, potential seagrass biomass production. This methodology of including the SAV growth model enables the COAWST framework to have a two-way feedback between hydrodynamic-biological coupling. Figure 1 describes the coupling process between different modules schematically.

10

3. Model Setup

3.1 Idealized test case

The implementation of the SAV growth model within the COAWST framework is first tested on an idealized domain. The test case consists of an idealized rectangular domain of 9.2 km width and 9.8 km length with a 1 m deep

15 basin. The number of interior domain points are 90 in the x-direction and 98 in the y-direction with 10 vertical sigma layers. The resulting domain has a grid resolution of 100 m by 100 m in horizontal and 0.1 m in the vertical (this varies with water level). A rectangular vegetation bed extends from the north boundary of the domain southward 8 km, with a width of 1.8 km, centered in the domain (Figure 3). The ROMS barotropic and baroclinic time steps are 0.05 s and 1 s respectively. The bed roughness is set to z_o =1.5 mm. The k − ε turbulence model is implemented following the

20 GLS method (Warner et al., 2005). The initial AGB, BGB and EPB in the vegetation bed are set to be 90, 15 and 0.01 mmol N/m^2 respectively. The vegetation density, height, diameter and thickness are initialized to be 400 stems/m^2, 0.19 m, 1.0 mm and 0.1 mm respectively. The vegetative drag coefficient (C$_D$) is set to be 1 (typical value for a cylinder at high Reynolds number). The imposed surface wind speed is 3 m/s from the north to induce a wave field. The surface air pressure is initialized as 101.3 kPa. The kinematic surface solar shortwave radiation is set to an

25 amplitude of 500.0 W/m^2 with a 24-hour period. The kinematic surface longwave radiation flux is set to zero (W/m^2). The surface air temperature varies between 1.5 ℃ to 18.5 ℃ over a yearly period. The surface solar downwelling spectral irradiance just beneath the sea surface is set following Gregg and Carder (1990). The cloud fraction is set to be zero. The bulk flux parameterizations in COAWST for surface wind stress and surface heat flux are based on the COARE code (Fairall et al. (1996a, 1996b) and Liu et al. (1979)).

30 The model is forced by oscillating the water level on the northern boundary with a tidal amplitude of 0.25 m and a period of 12 hours. Northern boundary conditions include a water temperature variation between 1.5 ℃ to 18.5℃ over an yearly period. Salinity and NO_3 at the northern boundary are set to 35 psu and 20 mmol N/m^3 respectively, and we impose a suspended sediment concentration of 0.5 g/L as well. The northern boundary condition for tracers is a radiation condition with nudging on a 6h timescale. For both flow and tracer fields (physical and biological), the

35 western and eastern boundaries have a gradient condition and the southern boundary is closed. The model setup for the idealized domain is simulated for 60 days and the model output is averaged over each day.

11

3.2 Realistic test case: West Falmouth Harbor, Massachusetts, USA

del Barrio et al. (2014) used an offline coupling of the COAWST model with a bio-optical seagrass model (Zimmerman et al., 2003) to study the influence of nitrate loading and sea-level rise on seagrass presence/absence in West Falmouth Harbor, Massachusetts, USA. Nitrate concentrations in groundwater exceeded 200 µM due to a

5 wastewater treatment plant in the watershed, however recent mitigation is expected to eliminate the nitrate load in the future. The model of del Barrio et al. (2014) used the biogeochemical results to generate spectral irradiance fields which were then passed to the bio-optical model. While useful for investigating the interaction between phytoplankton dynamics, light climate, and potential seagrass coverage, that model did not account for the interaction of seagrass with water column and sediment nitrogen pools, or hydrodynamics. Therefore, we tested the fully coupled

10 hydrodynamic, biogeochemical, and vegetation model using the same hydrodynamic and biogeochemical model setup (Ganju et al., 2012 and del Barrio et al., 2014), but with the full vegetative interaction implemented. Briefly, the model is forced with tides at the western boundary, groundwater and nitrate loading at the eastern boundary, and solar irradiance at the air-sea boundary. Further details on the model setup are given by Ganju et al. (2012) and del Barrio et al. (2014). The hydrodynamic and biogeochemical (e.g. chlorophyll concentrations, light attenuation) results were

15 assessed in those studies. In this work, we test the ability of the coupled model to reproduce the present-day spatial pattern of seagrass presence, with growth and persistence expected in the outer harbor, and dieback in the inner harbor, where nitrate loading, phytoplankton growth, and light attenuation are highest. The initial SAV properties include a plant height of 0.195 m, plant density of 110 stems/m^2, plant diameter of 0.001 m, and plant thickness of 0.0001 m. The vegetative drag coefficients C_D in the flow model and the wave model are set to 1 (typical value for a cylinder at

20 high Reynolds number). We utilize the SAV growth model parameters described in Table 1. The model setup for West Falmouth Harbor (Section 3.2) is simulated for 56 days, beginning 2 July 2010 (Ganju et al., 2012).

4 Results and Discussion

4.1 SAV, sediment, and hydrodynamics in the idealized test case

25 Simulations of the coupled hydrodynamic-biogeochemical-SAV model revealed the integrated nature of estuarine dynamics in response to submerged macrophytes. In these simulations, SSC was imposed at the northern open boundary at concentrations of 0.5 g/L (and zero g/L within the bed), resulting in a decline in SSC as one moves towards the southern boundary (Fig. 4a). This distribution of SSC input results in an increase in light attenuation (K_{dpar}=30.0 m^{-1}) in the region close to the northern boundary (0.0 km), while background conditions prevail in the

30 southern reaches (Fig. 4b). In Fig. 4b, SSC input from the northern boundary causes a decrease in light availability within the modelled SAV region between the open boundary in the north and about 2.4 km into the SAV bed. Consequently, these sub-optimal light conditions in the northern 2.4 km of the SAV bed cause AGB to decrease from its initial value of 90.0 millimoles N/m^2 to 30.0 millimoles millimoles/m^2 (Fig. 5a). Boundary effects associated with SSC inputs are substantially muted in the region between 2.4 km and 8.0 km within the SAV bed (Figs. 4&5), where

35 in-bed SSC concentrations are much lower than those outside the bed at the same distance from the boundary. As a consequence, where AGB biomass increases from its initial value of 90.0 millimoles N/m^2 to 150.0 millimoles N/m^2 over the course of the simulation. Increases in SAV biomass within the bed during the simulation led to increases in

12

SAV density and height, where SAV density increased from its initial value of 400 stems/m^2 to of 810 stems/m^2 owing to favourable light conditions from y=2.4 km to y=8.0 km. Thus, the model captured the role of SAV in resisting SSC transport into the bed, allowing for greater light availability and an increase in growth rates and biomass accumulation.

5 The temporal evolution of SAV biomass in response to the SSC input at the northern boundary further emphasizes the self-stimulating role of SAV in the idealized simulations. A comparison of model simulations at two locations within the initially described SAV bed of the idealized domain (indicated in Fig. 5a and corresponding to y=0.1 km and y=4.5 km from the northern boundary) reveal that close to the northern boundary (y=0.1 km), the daily averaged light attenuation remains high (above 30 m^{-1}) over the 60-day period (Fig. 5a). At y=0.1 km, the increased light attenuation in the northern location corresponds to the lack of light availability and this causes a decay of AGB

10 from its initial value of 90.0 millimoles N/m^2 to 30.0 millimoles N/m^2. (Fig. 5b). This decay in AGB over the 60-day period at y=0.1 km (SAV dieback), contrasts sharply with the AGB increases inside the SAV bed at the southern location (y=4.5 km), where light attenuation is lower because sediments have not penetrated the SAV bed, allowing for higher SAV growth rates. The higher SAV growth rate inside the SAV bed at y=4.5 km can be observed (Fig. 5c) by looking at the net primary production of SAV ($\rho_s - \delta_s - \varepsilon_s$). At this location (y=4.5 km), the SAV growth rate

15 increases over the 60-day period while it keeps decreasing in the northern location (y=0.1 km). Due to the higher SAV growth inside the SAV bed (y=4.5 km), the SSC in the bottom cell remains low (Fig. 5d) and at y=0.1 km due to the SAV dieback, the sediment concentration in the water column stays high and above 0.25 g/L.

As mentioned above, the SSC input on the northern boundary of the idealized domain causes a region of sub-optimal light conditions that lead to the SAV dieback; while the SAV growth occurs in the remaining bed where

20 favourable light conditions exist. The effect of change in SAV density and height on the hydrodynamics and morphodynamics at the end of the simulation can be demonstrated by using the same idealized domain. To this end, two transects are chosen that are along the length of the SAV bed and extend from the northern boundary towards the southern boundary. The transects are chosen inside at x=1.8 km (outside of the SAV bed) and at x=4.8 km (inside of the SAV bed). The depth-integrated SSC and bottom stresses averaged on the 60th day in the transect (Fig. 7a) outside

25 of the SAV bed show that the profile of bottom stress follows the distribution of SSC along the transect. In Fig. 7a, a 0.2 N/m^2 of peak bottom stress is obtained at x=1.8 km (outside of the SAV bed) that corresponds to a depth-averaged SSC of 0.31 g/L. On the other hand, the transect within the SAV bed (Fig. 7b) shows that the region where SAV dieback has occurred (between 0.0 km to 2.4 km) corresponds to increased bottom stresses (0.13 N/m^2 at the north most location and a corresponding SSC of 0.26 g/L) while the region where the SAV growth has occurred, the bottom

30 stresses are close to zero (i.e. from 2.4 km and onwards).

The simulation of the idealized domain demonstrates the capability of the modelling framework to perform two-way feedbacks between hydrodynamics, sediment and biological dynamics. The SSC input in the northern boundary affects the light attenuation in the domain and causes SAV dieback close to the northern boundary. The SAV grows in the region where favourable light conditions exist. The SAV dieback leads to increased bottom stresses

35 while the growth of SAV leads to a decrease in bottom stresses; illustrating the fact that the SAV act as bottom sediment stabilizers by reducing SSC.

13

4.2 SAV growth in West Falmouth Harbor

The present-day simulation of seagrass dynamics reproduces the patterns of chlorophyll (via phytoplankton), light attenuation, and near-bottom PAR simulated by del Barrio et al., 2014. Nitrate loading from shoreline point sources led to increased phytoplankton growth indicated by increased chlorophyll and light attenuation in the landward,
5 northeast portion of the harbor (Fig. 8a,b), while bathymetric controls in the deeper central basin led to decreased near-bottom PAR (Fig. 8c). Peak AGB exceeds 100 millimoles N m^{-2}, while seagrass presence begins towards decline in the inner harbor and in the central basin as expected. Intertidal areas around the periphery of the harbor are devoid of AGB due to the enforced masking of areas with intermittent wetting and drying.

Time-series of these parameters (Fig. 9) from selected outer and inner harbor locations over the first 22 days
10 demonstrate the diurnal variability, as well as the rapid loss of AGB in the inner harbor due to the local nitrate loading, phytoplankton proliferation, and degraded light climate. The sizeable diurnal variability in AGB (Fig. 9d) appears to be an artifact of production/respiration formulations that are based on seasonal responses to environmental forcing, rather than diurnal responses to solar irradiance. Future modifications could attenuate this variability by utilizing daily averaged environmental forcing, or modifying the frequency of biomass updating.

15 The modelling framework developed in this work can be used to create hypothetical scenarios to estimate future environmental responses. For example, we ran the model setup of West Falmouth Harbor described in section 3.2 with no nitrate loading, to simulate a hypothetical scenario where the groundwater input has no influence from the wastewater treatment plant (unimpacted past or future scenario). The elimination of nitrate loading results in negligible changes in the outer harbor, but greatly reduces chlorophyll and light attenuation in the inner harbor (Fig. 10a, b), while
20 increasing the near-bottom PAR (Fig. 10c). Peak AGB responds to the decreased chlorophyll and increased light attenuation with an increase in the inner harbor (Fig. 10d). This implementation represents an incremental improvement to the prior modelling exercise (Ganju et al., 2012 and del Barrio et al., 2014), because the interaction between SAV and the nitrogen pools are explicitly accounted for. For example, this model can now be used to test how changes in seagrass coverage influence nitrogen retention within the estuary, or export to the coastal ocean.
25 Further, the introduction of seagrass kinetics will allow for investigation of water column oxygen budgets with and without seagrass, under present and future scenarios.

4.3. Model evaluation in West Falmouth Harbor

30 In order to qualitatively evaluate the seagrass growth model, we have compared the modeled results with observations by del Barrio et al. (2014) that measured the extent of seagrass coverage in West Falmouth Harbor (red outline in Fig. 11). The field data is only available for the northern region of WFH where the model-data comparisons are performed. The model results are compared by extracting the peak above ground biomass (AGB) on 14th day of the simulation and normalized with the initial above ground biomass. The ratio of AGB/AGB$_{initial}$ is considered as a representative
35 of seagrass growth. We assume that for AGB/AGB$_{initial}$ > 1, there is a potential for seagrass growth and for AGB/AGB$_{initial}$ <1, the conditions are unfavorable for seagrass growth. In fig 11, the model and field data show a 89% agreement to determine the seagrass growth or dieback. The western region of outer harbor shows seagrass growth potential and agrees with the extent that the seagrass coverage is observed. In the eastern region, the field data shows

14

no seagrass coverage and the model also predicts potential seagrass dieback. The model predicts seagrass dieback because of nitrate loading from shoreline point sources that leads to increased chlorophyll and light attenuation (figures 8a, b). The model and observations do not compare well in the central basin of outer harbor where the model shows seagrass dieback potential while the field data shows presence of seagrass. In the central basin, the field data shows the presence of seagrass while its density remains low in this region. On the other hand, the modelled seagrass suffers dieback due to the bathymetric controls in the deeper central basin (decreased near-bottom PAR Fig. 8c).

Direct estimates of above ground SAV biomass have also been recently made in West Falmouth Harbor (Hayn et al., unpublished data). Although these measurements were not made during the same year as our simulations (measurements in 2006, 2007, 2013; model 2010), the mean above ground biomass measured in the outer harbor of 49.5 (June 21-July 6 2006), 45.3 (June 6-19 2007), and 41.5 g C m^{-2} (July 15-19 2013) is consistent with the range of model simulations during a comparable period (July 2-19) in the outer (28.1 to 51.1 g C m^{-2}) and middle (14.9 to 37.4 g C m^{-2}) harbors. The July 2-19 model range of 45.7 to 156.3 mmol N m^{-2} across the middle and outer harbor is also consistent with annual mean *Z. marina* biomass (10-88 mmol N m^{-2}) reported in nearby shallow systems on Cape Cod (Hauxwell et al. 2003) assuming a literature-based average that above ground SAV biomass is 1.5% N. The range in the model is computed based on the minimum and maximum values of AGB during the 18 day simulation period.

4.4 Limitations of SAV growth model and Future Work

While this modelling approach represents an advance in modelling coupled biophysical processes in estuaries, there are limitations that must be addressed in future work:

1. The modelling of SAV dieback/growth scenarios may require long-term simulations on decadal timescales (Carr et al., 2018). However, the short model time step limits the duration of such simulations. The time step size is of the order of seconds (typical of 3-D ocean models) and this combined with the fact that the presence of SAV in the hydrodynamic model further limits time step size (due to hydrodynamic stability constraints); overall limits the applicability of the model to be utilized from monthly to annual time scales at this juncture.

2. The biomass equations described in Section 2.3 are formulated for seasonal time scales and are being used in the model implementation at every ocean model time step. This leads to large daily variations in above and below ground biomass that do not likely occur in the environment, although diel variations on SAV growth have been measured in situ (Kemp et al. 1987). Hence, with the current formulations, the output from the biomass model needs to be analyzed as a daily averaged quantity.

3. The current implementation of the SAV growth model is limited to only one SAV species. However, it should be extended to include multiple SAV species to investigate competition under variable salinity and to make the model applicable to a wider variety of locations.

5 Conclusions

The present study adds to the open source COAWST modelling framework by implementing a SAV growth model. Based on the change in SAV biomass (above ground, below ground) and epiphyte biomass, SAV density and height evolve in time and space and directly couple to three-dimensional water-column biogeochemical,

15

hydrodynamic, and sediment transport models. SAV biomass is computed from temperature, nutrient loading and light predictions obtained from coupled hydrodynamics (temperature), bio-geochemistry (nutrients) and bio-optical (light) models. In exchange, the growth of SAV sequesters or contributes nutrients from the water column and sediment layers. The presence of SAV modulates current and wave attenuation and consequently affects modelled
5   sediment transport and fate. The resulting modelling framework provides a two-way coupled SAV-biogeochemistry-hydrodynamic and morphodynamic model. This allows for the simulation of the dynamic growth and mortality of SAV in coastal environments in response to changes in light and nutrient availability, including SAV impacts on sediment transport and nutrient, carbon, and oxygen cycling. The implementation of the model is successfully tested in an idealized domain where the introduction of sediment in the water column (SSC) at one end of the domain
10   provides sub-optimal light conditions that causes SAV dieback in that region. The model was applied to the temperate estuary of West Falmouth Harbor, where simulations show the coupled effect of enhanced nitrate loading in the inner harbour leading to poor light conditions for the SAV to grow; thus modelling the physical effect of eutrophication leading to the loss of SAV habitat. Among other applications, in future, the model will be used assess the effects of sea level rise scenarios that limit light availability and potentially cause the loss of SAV habitat.

6 Code availability

The implementation of the SAV growth model has been implemented in the Coupled Ocean Atmosphere Waves Sediment-Transport Modeling System (COAWST v3.4). This particular version is available for download at: https://www.sciencebase.gov/catalog/item/5f15d69082cef313ed81996a. Users are encouraged to download COAWST distributed through the USGS code archival repository. It is available for download on https://code.usgs.gov/coawstmodel/COAWST. The COAWST distribution files contain source code derived from ROMS, SWAN, WRF, MCT and SCRIP, along with the Matlab code, examples and a User's Manual.

The major code development that was done for this project is contained within the COAWST folder on the following path.

"https://code.usgs.gov/coawstmodel/COAWST/blob/master/ROMS/Nonlinear/Biology/"

This folder contains several methods of computing water column biogeochemistry. Other than the I/O component of our implementation, the algorithmic development in this study only modifies two files on this path: "estuarybgc.h" and "sav_biomass.h". The file "sav_biomass.h" contains all the newly added equations for the growth of SAV based on the nutrient loading in the water column. The forcings to the SAV growth model (temperature, light, nutrient availability, exchanges nutrients, detritus, dissolved inorganic carbon, and dissolved oxygen) are provided through the file "estuarybgc.h" that calls "sav_biomass.h". The file "estuarybgc.h" solves for the water column biogeochemistry and was based on existing modelling framework developed by Fennel et al. (2006) (also coded as "fennel.h").

Other important paths that existed in the framework prior to the current modeling effort but are being used in the modeling process include:

1. "https://code.usgs.gov/coawstmodel/COAWST/blob/master/ROMS/Nonlinear"-

The main kernel of the 3-D non-linear Navier-Stokes equations is contained within this part and links all the submodels: biological, vegetation and sediment models.

2. "https://code.usgs.gov/coawstmodel/COAWST/blob/master/ROMS/Nonlinear/Vegetation/"

The kernals that account for seagrass-hydrodynamics interactions.

3. "https://code.usgs.gov/coawstmodel/COAWST/blob/master/ROMS/Nonlinear/Sediment/"

The kernals that account for sediment transport.

7 Data availability

The model data was released as per the USGS model data release policy and separate digitial object identifiers were created as part of the release (https://www.usgs.gov/products/data-and-tools/data-management/data-release). The model output can be accessed through sciencebase entries for the idealized test case simulation (Kalra and Ganju, 2019) and West Falmouth Harbor simulations (Ganju and Kalra, 2019). For each of the model data releases, separate landing pages are constructed and the model data can be either accessed through thredds server or directly downloaded in netcdf format. The model output from the idealized test case simulation (Kalra and Ganju, 2019) can be accessed via thredds server or directly downloaded in netcdf format from this link:

https://www.sciencebase.gov/catalog/item/5d3b4d32e4b01d82ce8d77f5

The model output from the West Falmouth Harbor simulation (Ganju and Kalra, 2019) can be accessed via thredds

1

8 Author contribution

T. S. Kalra implemented the SAV growth model in the COAWST framework. J. Testa provided guidance on the
10 mechanistic processes affecting the growth of SAV from biomass parameterizations and developed linkages between
the SAV growth model and the water-column biogeochemical model. N. K. Ganju developed the test case and the
realistic domain case. T. S. Kalra and N. K. Ganju performed the data analysis from the output of the test cases and
were responsible for model data release. The manuscript was prepared with contributions from all co-authors.

15 **9 Disclaimer**

This draft manuscript is distributed solely for purposes of scientific peer review. Its content is deliberative and pre-
decisional, so it must not be disclosed or released by reviewers. Because the manuscript has not yet been approved for
publication by the U.S. Geological Survey (USGS), it does not represent any official USGS finding or policy. Any
use of trade, firm, or product names is for descriptive purposes only and does not imply endorsement by the U.S.
20 Government.

10 Acknowledgements

11 References

Beudin, A., Kalra, T. S., Ganju, N., K., and Warner, J.C.: Development of a Coupled Wave-Current-Vegetation
Interaction, Computers & Geosciences, 100, 76-86, 2017.
35 Bissett, W.P., Carder, K.L., Walsh, J.J., Dieterle, D.A.: Carbon cycling in the upper waters of the Sargasso Sea: II.
Numerical simulation of apparent and inherent optical properties, Deep-Sea Research Part 1: Oceanographic Research
Papers, 46, 271-317, 1999.

Burkholder, J.M., Tomasko, D.A., Touchette, B.W.: Seagrasses and eutrophication, Journal of Experimental Marine Biology and Ecology, 350, 46-72, 2007.

Booij N., Ris, R.C., and Holthuijsen, L.H.: A third-generation wave model for coastal regions, Part I, Model description and validation, Journal of Geophysical Research C4, 104, 7649-7666, 1999.

5   Cabello-Pasini, A., Muniz-Salazar, R., Ward, D.H.: Annual variations of biomass and photosynthesis in Zostera marina at its southern end of distribution in the North Pacific, Aquatic Botany, 76, 31-47, 2003.

Carr, J., D'Odorico, P., McGlathery, K., Wiberg, P.: Stability and bistability of seagrass ecosystems in shallow coastal lagoons: role of feedbacks with sediment resuspension and light attenuation, Journal of Geophysical Research, 115, G03011, 2010.

10   Carr, J. A., P. D'Odorico, P., McGlathery, K.J., and Wiberg, P.L.: Stability and resilience of seagrass meadows to seasonal and interannual dynamics and environmental stress, Journal of Geophysical Research, 117, G01007, 2012.

Carr, J. A., P. D'Odorico, P., McGlathery, K.J., and Wiberg, P.L.: Modeling the effects of climate change on eelgrass stability and resilience: future scenarios and leading indicators of collapse, Marine Ecology Progress Series, 448, 289-301, 2012.

15   Carr, J., Mariotti, G., Fahgerazzi, S. McGlathery, K.,and Wiberg, P.: Exploring the Impacts of Seagrass on Coupled Marsh-Tidal Flat Morphodynamics. Frontiers of Environmental Science, 6, 92, 2018.

Cerco, C.F. and Moore, K.: System-wide submerged aquatic vegetation model for Chesapeake Bay, Estuaries, 24, 522-534, 2001.

Chassignet, E.P., Arango, H.G., Dietrich, D., Ezer, T., Ghil, M., Haidvogel, D.B., Ma, C.-C., Mehra, A.,

20   Paiva, A.M., Sirkes, Z. Dynamics of Atmospheres and Oceans 2000, Vol. 32, pp. 155-183.

Cossarini, G., Querin, S., Solidoro, C., Sannino, G., Lazzari, P., Biagio, V. and Bolzon, G., Development of BFMCOUPLER (v1.0), the coupling scheme that links the MITgcm and BFM models for ocean biogeochemistry simulations, Geosci. Model Dev., 10, 1423–1445, https://doi.org/10.5194/gmd-10-1423-2017, 2017

Costello, C.T. and Kenworthy, W.J., Twelve-Year Mapping and Change Analysis of Eelgrass (Zostera marina)

25   Areal Abundance in Massachusetts (USA) Identifies Statewide Declines, Estuaries and Coasts, Vol, 34:232–242, 2011.

del Barrio, P., Ganju, N. K., Aretxabaleta, A. L., Hayn, M., García, A., and Howarth, R. W.: Modeling future scenarios of light attenuation and potential seagrass success in a eutrophic estuary, Estuarine, Coastal and Shelf Science, 149, 13-23, 2014.

30   Everett, J.D., Baird, M.E., Suthers, I.M.: Nutrient and plankton dynamics in an intermittently closed/open lagoon, Smiths Lake, south-eastern Australia: an ecological model, Estuarine, Coastal and Shelf Science, 72, 690-702, 2007.

Fairall, C.W., Bradley, E.F., Rogers, D.P., Edson J.B., and Young, G.S.: Bulk parameterization of air-sea fluxes for tropical ocean global atmosphere Coupled-Ocean Atmosphere Response Experiment, Journal of Geophysical Research, 101, 3747-3764, 1996a.

35   Fairall, C.W., Bradley, E.F., Godfrey, J.S., Wick, G.A., Edson, J.B., and Young, G.S.: Cool-skin and warm-layer effects on sea surface temperature, Journal of Geophysical Research, 101, 1295-1308, 1996b.

Fennel K., Wilkin, J., Levin, J. Moisan, J. O'Reilly, and D. Haidvogel, D.: Nitrogen cycling in the Middle Atlantic Bight:

results from a three-dimensional model and implications for the North Atlantic nitrogen budget, Global Biogeochemical Cycles, 20, GB3007, 2006.

5 Ganju, N.K., Hayn, M., Chen, S.N., Howarth, R.W., Dickhudt, P.J., Aretxabaleta, A.L., Marino, R.: Tidal and groundwater fluxes to a shallow, microtidal estuary: constraining inputs through field observations and hydrodynamic modeling, Estuaries Coasts, 35, 1285-1298, 2012.

Ganju, N.K., Testa, J.M., Suttles, S.E., Aretxabaleta, A.L.: Spatiotemporal variability of light attenuation and net ecosystem metabolism in a back-barrier estuary, Biogeosciences Discussions: 10.5194/bg-2018-5335.

10 Ganju, N.K., and Kalra, T.S., Numerical model of Submerged Aquatic Vegetation (SAV) growth dynamics in West Falmouth Harbor: U.S. Geological Survey data release, https://doi.org/10.5066/P998IJGG, 2019.

Gallegos, C.L., Werdell, P.J., McClain, C.R., 2011.: Long-term changes in light scattering in Chesapeake Bay inferred from Secchi depth, light attenuation, and remote sensing measurements, Journal of Geophysical Research, 116, C00H08, 2011.   Gregg, W.W. and Carder, K.L.: A simple spectral solar irradiance model for cloudless maritime

15 atmospheres, Limnology and. Oceanography, 35(8), 1657-1675, 1990.

Haidvogel, D.B., Arango, H.G., Hedstrom, K., Beckmann, A., Malanotte-Rizzoli, P., Shchepetkin, A.F. Model evaluation experiments in the North Atlantic Basin: simulations in nonlinear terrain-following coordinates. Dynamics of Atmosphere Oceans 2000, Vol. 32, pp. 239–281.

Haidvogel, D.B., Arango, H.G., Budgell, W.P., Cornuelle, B.D., Curchitser, E., Di Lorenzo E., Fennel, K., Geyer,

20 W.R., Hermann, A.J., Lanerolle, L., Levin, McWilliams, J.C., Miller, Moore, A.M., Powell, T.M., Shchepetkin, A.F., Sherwood, C.R., Signell, R.P., Warner, J.C. and Wilkin, J.: Ocean forecasting in terrain-following coordinates: Formulation and skill assessment of the Regional Ocean Modeling System, Journal of Computational Physics, 227, 3595-3624, 2008.

Hamberg, J., Findlay, S.E.G., Limburg, K.E., Diemont, S.A.W.: Post-storm sediment burial and herbivory of

25 Vallisneria americana in the Hudson River estuary: mechanisms of loss and implications for restoration: Storm burial and herbivory of Vallisneria, 25, 2017.

Hauxwell, J., Cebrian, J., and Valiela, I., Eelgrass Zostera marina loss in temperate estuaries: relationship to land-derived nitrogen loads and effect of light limitation imposed by algae, Vol.247:59-73, 2003.

Hayn, M., Howarth, R.W., Marino, M., Ganju, N., Berg, P., Foreman, K., Giblin, A, McGlathery, K.: Exchange of

30 nitrogen and phosphorus between a shallow lagoon and coastal waters, Estuaries Coasts 37, S63-S73 (Suppl. 1), 2014.

Hemming, M.A., and Duarte, C.M.: Seagrass Ecology, Cambridge University Press, 2000.

Hipsey, M.R., and Hamilton, D.P.: Computational Aquatic Ecosystem Dynamic Model: CAEDYM v3 Science Manual. Centre for Water Research, 2008.

35 Jarvis, J.C., M.J. Brush, and K.A. Moore. 2014.Modeling loss and recovery of Zostera marina beds in the Chesapeake Bay: the role of seedlings and seed-bank viability. Aquatic Botany,113: 32-45.

Kalra, T.S.; Li, X.; Warner, J.C.; Geyer, W.R.; Wu, H. Comparison of Physical to Numerical Mixing with Different Tracer Advection Schemes in Estuarine Environments. Journal of Marine Science and Engineering, 2019, Vol. 7, 338.

Kalra, T.S., and Ganju. N. K., 2019, Idealized numerical model for Submerged Aquatic Vegetation (SAV) growth dynamics: U.S. Geological Survey data release, https://doi.org/10.5066/P973NL8J.

Kemp, W., Murray, L., Borum, J., and Sand-Jensen, K.: Diel growth in eelgrass *Zostera marina*, Marine Ecology Progress Series, 41, 79-86, 1987.

Kennish, M.J., Sakowicz, G.P. and Fertig, B.: Recent Trends of Zostera marina (Eelgrass) in a Highly Eutrophic Coastal Lagoon in the Mid-Atlantic Region (USA), Open Journal of Ecology, 6, 243-253, 2016.

Krause-Jensen, D., Middelboe, A.L., Sand-Jensen K, Christensen P.B.: Eelgrass, Zostera marina, growth along depth gradients: upper boundaries of the variation as a powerful predictive tool. Oikos, 91, 233-244, 2000.

Larkum, A. W., Orth, R. J., Duarte, C. M.: Seagrasses: Biology, Ecology and Conservation, Springer, 2006.

Liu, W.T., Katsaros, K.B., and Businger J.A.: Bulk parameterization of the air-sea exchange of heat and water vapor including the molecular constraints at the interface, Journal of Atmospheric Sciences, 36, 1722-1735, 1979.

Matsumoto, K., Tokos, K., Huston, A., and Joy-Warren, H.: MESMO 2: a mechanistic marine silica cycle and coupling to a simple terrestrial scheme, Geosci. Model Dev., 6, 477–494, https://doi.org/10.5194/gmd-6-477-2013, 2013.

Madden, C. J., Kemp, W. M..: Ecosystem Model of an Estuarine Submersed Plant Community: Calibration and Simulation of Eutrophication Responses: Estuarine Research Foundation, 19, No. 2B, 457-474, 1996.

McGlathery, K.J., Sundback, K., Anderson, I.C.: Eutrophication in shallow coastal bays and lagoons: the role of plants in the coastal filter, Marine Ecology Progress Series, 348, 1-18, 2007.

Moore, K.A.: Influence of Seagrasses on Water Quality in Shallow Regions of the Lower Chesapeake Bay, Journal of Coastal Research, 162-178, 2004.

Nixon, S.W., Buckley, B., Granger, S., Bintz, J.: Responses of very shallow marine ecosystems to nutrient enrichment, Human Ecological Risk Assessment: An International Journal, 7, 1457-1481, 2001.

Shchepetkin, A.F., and McWilliams, J.C. The Regional Ocean Modeling System: A split-explicit, free-surface, topography-following coordinates ocean model, Journal of Ocean Modelling 2005, Vol. 9, pp. 347–404.

Shchepetkin, A.F., McWilliams, J.C., Computational Kernel Algorithms for Fine-Scale, Multiprocess, Longtime Oceanic Simulations, Handbook of Numerical Analysis 14, 121-183, 2009.

Sherwood, C.R., Aretxabaleta, A.L., Harris, C.K., Rinehimer, J.P., Verney, R., and Ferré, B., Cohesive and mixed sediment in the Regional Ocean Modeling System (ROMS v3.6) implemented in the Coupled Ocean–Atmosphere–Wave–Sediment Transport Modeling System (COAWST r1234), Geosci. Model Dev., 11, 1849–1871, https://doi.org/10.5194/gmd-11-1849-2018, 2018.

Sherwood, C.R., Signell, R.P., Warner, J.C., and Wilkin, J.: Ocean forecasting in terrain-following coordinates: formulation and assessment of the regional ocean modeling system, Journal of Computational Physics, 227, 3595-3624, 2008.

Short, F.T., and Neckles, H.A.: The Effects of Global Climate Change on Seagrasses, Aquatic Botany, 63, S0304-3770, 1999.

5

Smolarkiewicz, P.K. A fully multidimensional positive definite advection transport algorithm with small implicit diffusion. Journal of Computational Physics 1984, Vol. 54, pp. 325–362.

Terrados, J., Borum, J., Why are seagrasses important ? - Goods and services provided by seagrass meadows, 2006.

Thyng, K. M., Greene, C. A., Hetland, R. D., Zimmerle, H. M., & DiMarco, S. F.: True colors of oceanography. Oceanography, 29(3), 10., 2016.

Warner J.C., Sherwood, C.R., Signell, R.P., Harris, C.K., and Arango, H.G.: Development of a three-dimensional, regional, coupled wave, current, and sediment-transport model, Computer & Geosciences, 34, 1284-1306, 2008.

Warner J. C., Armstrong, B., R. He, R., and Zambon, J.B.: Development of a Coupled Ocean-Atmosphere-Wave-Sediment Transport (COAWST) Modeling System, Ocean Modelling, 35, 230-244, 2010.

Woodward, P., and Colella, P., The numerical simulation of two-dimensional fluid flow with strong shocks. Vol.54(1), pp. 115-173, 1984.Zaldívar, J.M., F.S. Bacelar, S. Dueri, D. Marinov, P. Viaroli, and E. Hernández-García. 2009. Modeling approach to regime shifts of primary production in shallow coastal ecosystems. Ecological Modelling 220: 3100-3110.

Zharova, N, A. Sfriso, A. Voinov, B. Pavoni. 2001. A simulation model for the annual fluctuation of Zostera Marina biomass in the Venice lagoon. Aquatic Botany 70:135-150.

Zimmerman, R.C.: A biooptical model of irradiance distribution and photosynthesis in seagrass canopies, Limnology and Oceanography, 48, 568-585, 2003.

5

10

15

20

25

6

Model variable	Equivalent symbol in source code	Description of terms
α	AGB	Above ground biomass
β	BGB	Below ground biomass
γ	EPB	Epiphyte biomass
μ_s	ua_{SAV}	Maximum potential growth rate (SAV)
ρ_s	pp_{SAV}	Primary production (SAV)
φ_s	$llmt_{SAV}$	Light availability (SAV)
ϑ_s	$nlmt_{SAV}$	Nutrient limitation (SAV)
λ_s	$lambda_{SAV}$	Self-shading term (SAV)
δ_s	$agar_{SAV}$	Active respiration (SAV)
ε_s	$agbr_{SAV}$	Above ground basal respiration (SAV)
$\omega_{s,1}$	agm_{SAV}	Above ground biomass mortality (SAV)
$\omega_{s,2}$	bgm_{SAV}	Below ground biomass mortality (SAV)
θ	PAR	Photosynthetic Active Radiation (PAR)
$\sigma_{s,1}$	$agbg_{SAV}$	Translocation of above ground biomass to below ground biomass (SAV)
$\sigma_{s,2}$	$bgbg_{SAV}$	Translocation of below ground biomass to above ground biomass (SAV)
μ_e	ua_{EPB}	Maximum potential growth rate (EPB)
ρ_e	pp_{EPB}	Primary production (EPB)
φ_e	$llmt_{EPB}$	Light availability (EPB)
ϑ_e	$nlmt_{EPB}$	Nutrient limitation (EPB)
λ_e	$lambda_{EPB}$	Self-shading term (EPB)
$\varepsilon_{e,1}$	$aresp_{EPB}$	Active respiration (EPB)
$\varepsilon_{e,2}$	$bresp_{EPB}$	Basal respiration (EPB)
ω_e	$mort_{EPB}$	Mortality (EPB)
$\tau_{e,1}$	grz_{EPB}	Loss of EPB due to grazing
$\tau_{e,2}$	epb_{slgh}	Epiphyte biomass due to the SAV sloughing loss
t	$dtdays$	Time step in days

Table 1: SAV growth model variable descriptions

5

10

Input parameter	Equivalent symbol in model	Description	Default value	Units
g_s	scl	SAV growth fraction	0.03	None
r_s	arc	SAV active respiration coefficient	0.01	dtdays^{-1}
$T_{s,o}$	T_{OPT}	Optimum SAV growth temperature	15.0	℃
$\lambda_{s,max}$	$\lambda_{SAV,max}$	Self-shading parameter for SAV leaves (maximum AGB)	475.0	millimoles N m^{-2}
l_s	$klmt$	Half-saturation for light limitation for SAV	100.0	E m^{-2} s^{-1}
$n_{s,1}$	kn_t	Half-saturation for nutrient limitation for plant roots	100.0	millimoles
$n_{s,2}$	kn_{wc}	Half-saturation for nutrient limitation for plant leaves	5.71	millimoles
p_s	$arsc$	Maximum fraction of photosynthesis, SAV respiration	0.1	None
c_s	$bsrc$	Maximum fraction of SAV BGB biomass respired	0.0015	None
h_s	rc	SAV basal respiration coefficient (AGB and BGB)	0.069	dtdays^{-1}
m_α	km_{ag}	SAV AGB mortality rate (sloughing)	0.0005	dtdays^{-1}
m_β	km_{bg}	SAV BGB mortality rate	0.005	dtdays^{-1}
g_e	scl_{EPB}	Epiphyte growth fraction	0.2	None
r_e	arc_{EPB}	Epiphyte active respiration coefficient	0.0633	dtdays^{-1}
$T_{e,o}$	$T_{EPB,opt}$	Optimum growth temperature for epiphytes	25.0	℃
$\lambda_{e,max}$	$\lambda_{EPB,max}$	Self-shading parameter for epiphytes (maximum EPB)	475.0	millimoles N m^{-2}
l_e	kl_{EPB}	Half-saturation for light limitation for SAV	50.0	E m^{-2} s^{-1}
n_e	kn_{EPB}	Half-saturation for nutrient limitation for SAV	10.0	millimoles
p_e	$arsc_{EPB}$	Maximum fraction of photosynthesis, EPB active respiration	0.01	None
c_e	$brsc_{EPB}$	Maximum fraction of SAV BGB biomass respired	0.0015	None
h_e	rc_{EPB}	SAV basal respiration coefficient (AGB and BGB)	0.069	dtdays^{-1}
m_e	$kmort_{EPB}$	Mortality rate for epiphytes if no sloughing	0.001	dtdays^{-1}
$z_{e,max}$	$grz_{EPB,max}$	Maximum grazing rate on epiphytes	0.1	dtdays^{-1}
z_e	$grzk_{EPB}$	Grazing coefficient on epiphytes	0.01	None
k_1	kd_{trans}	Downward translocation coefficient	0.1	None
k_2	ku_{trans}	Upward translocation coefficient	0.02	None
m_f	mx_{frc}	Upward translocation coefficient	0.02	None

Table 2: SAV growth model input parameter descriptions and their values

5

5

Figure 1: Schematic showing the coupling of SAV growth module implementation in COAWST model.
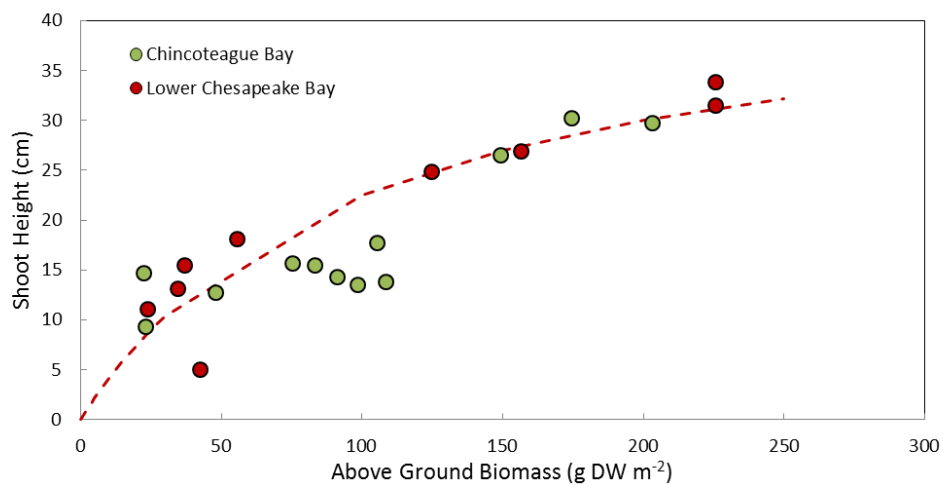
10

15

9

Figure 2: Empirical relationships between above ground biomass and SAV shoot height for Z. marina populations in polyhaline regions of Chesapeake Bay and Chincoteague Bay. Data from Moore et al. 2004 and Ganju et al. 2018.
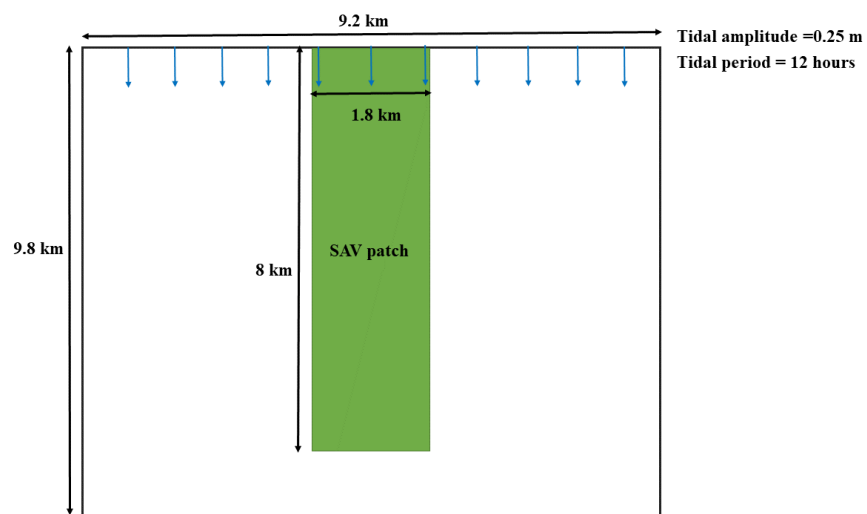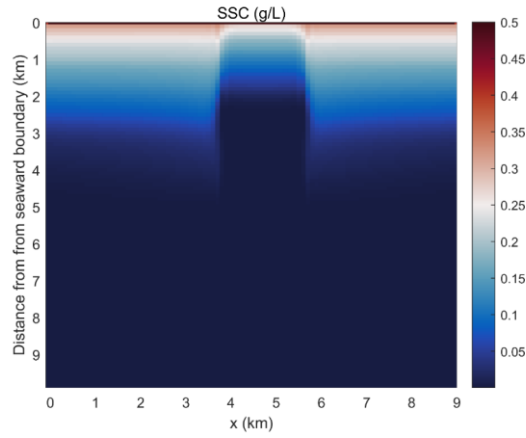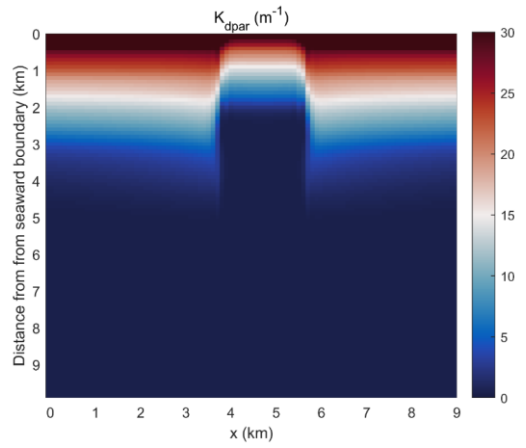
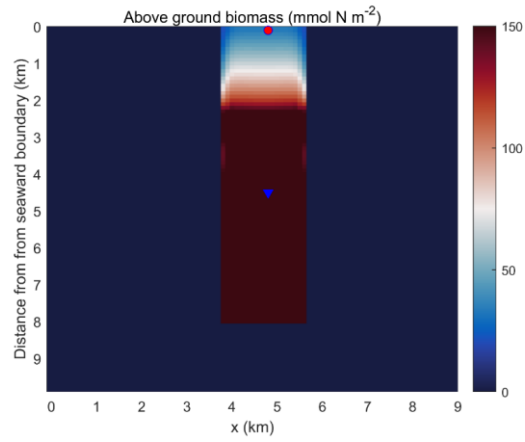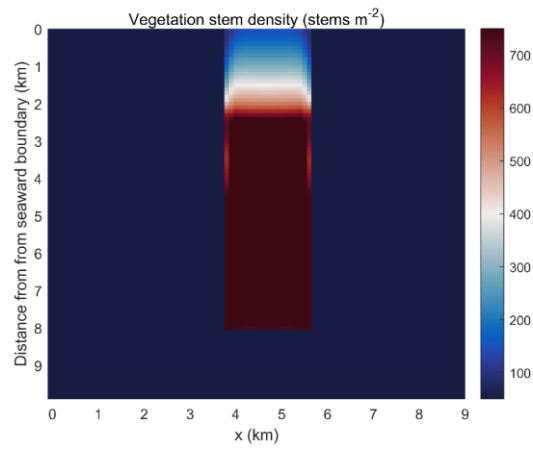**Figure 3: Planform view of the idealized test domain simulation.**

(a)

(b)

Figure 4: Planform view of (a) depth-integrated SSC, (b) light attenuation averaged over the last day of the simulation in the idealized domain.

(a)

(b)

Figure 5: Planform view of (a) above ground biomass and (b) vegetation stem density averaged over the last day of the simulation in the idealized domain. Red dot and blue triangle represent two points that are located at 0.1 km and 4.5 km into the SAV bed respectively.

(a)

(b)

(c)

(d)

5

Figure 6: Time-series of a) light attenuation,b) above ground biomass, c) net primary production of SAV
$(\rho_s - \delta_s - \varepsilon_s)$**, and d) SSC in the bottom cell averaged every day from the two locations identified in Fig. 5a.**

10

(a)

(b)

Figure 7. Magnitude of bottom stress (left) and depth-integrated SSC (right) at the end of the simulation plotted along the y axis of the idealized domain at two locations, including one outside (x=1.8 km; panel a) and one inside the SAV bed (x=4.8 km, panel b).
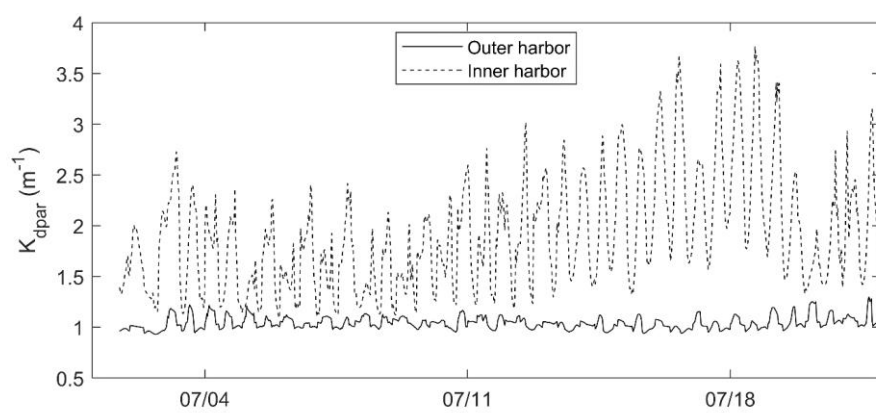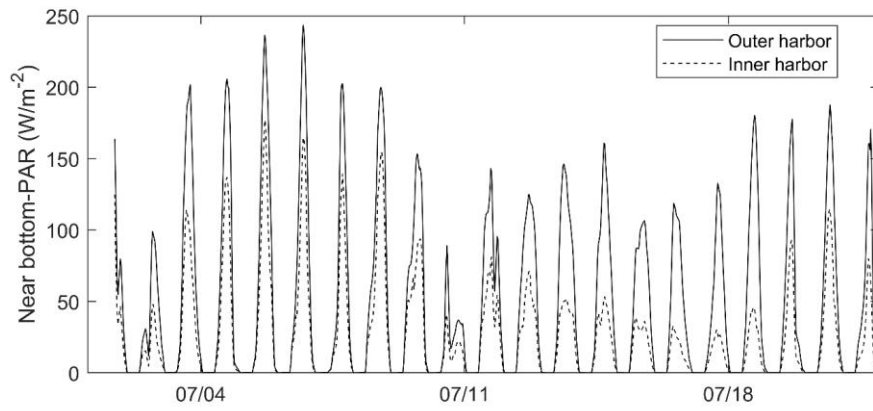
(a) (b)

(c) (d)

Figure 8. Mean over 22 days of a) depth-averaged chlorophyll, b) light attenuation, c) near-bottom PAR, and d) peak above ground biomass at day 14 of the simulation. Red circle indicated outer harbor (left) and blue triangle indicated inner harbor (right) points for time-series data in Figure 9.
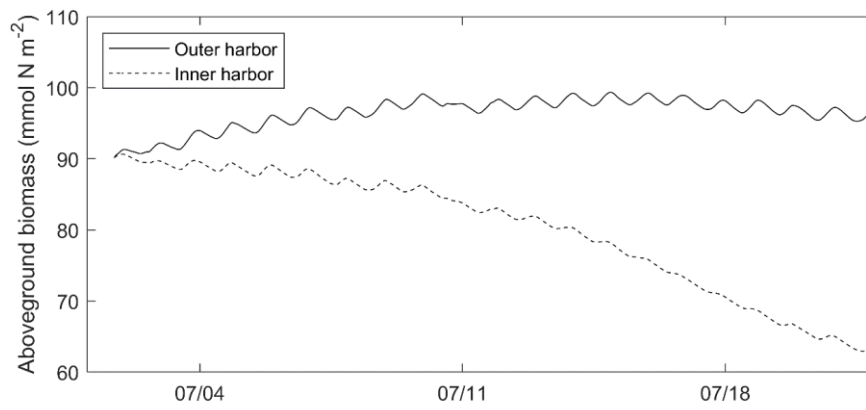
5

10

16

(a)

(b)

5

(c)

(d)

Figure 9. Time-series of a) chlorophyll, b) light attenuation, c) near-bottom PAR, and d) above ground biomass from outer and inner harbor locations identified in Figure 6.

(a)   (b)
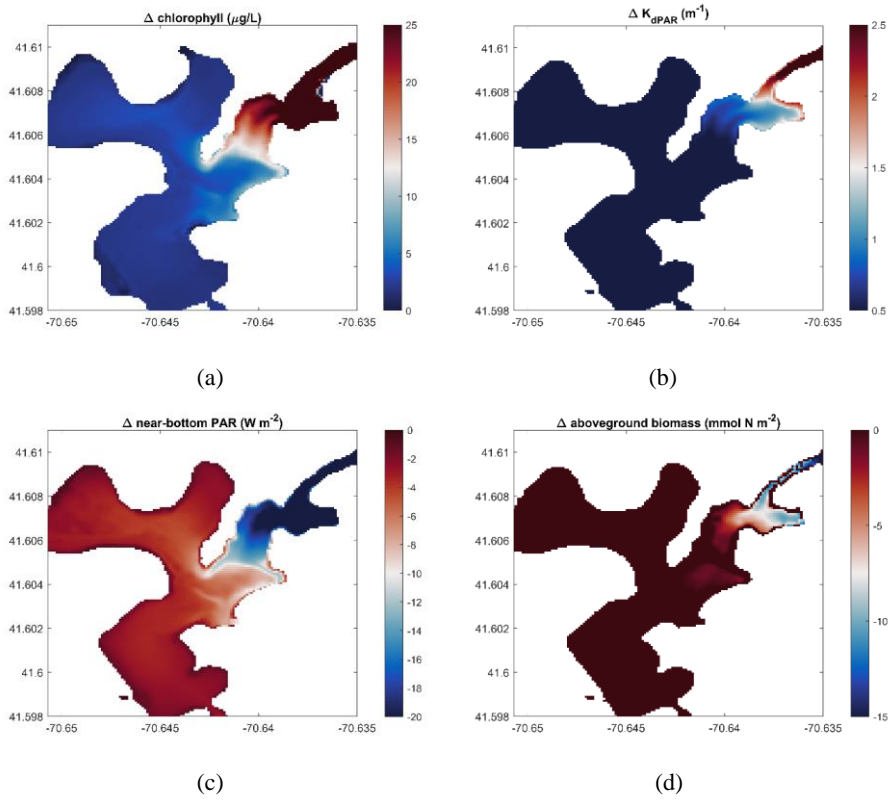

(c)   (d)

5

Figure 10. Change in outcomes between impacted and non-impacted scenario (nitrate loading scenario – no loading scenario). Difference in mean over 22 days of (a) depth-averaged chlorophyll, (b) light attenuation, (c) near-bottom PAR, and (d) peak above ground biomass at day 14 of the simulation.
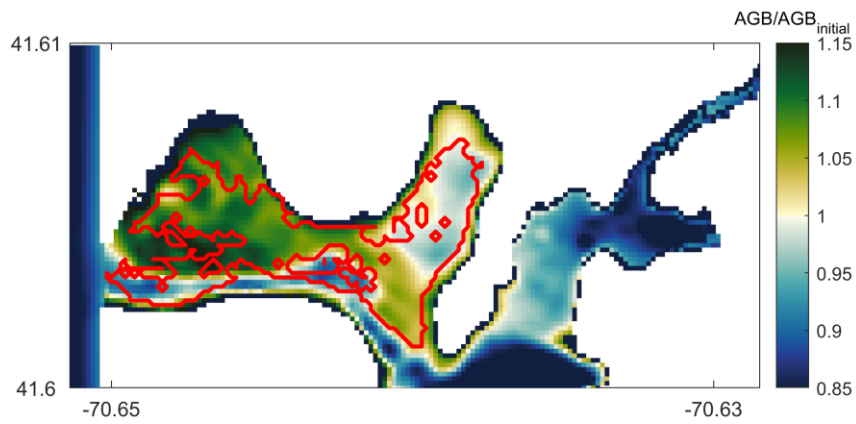
10

15

19

Fig 11: Modeled AGB/AGB$_{initial}$ (above ground biomass) distribution compared with field data showing seagrass coverage extent (red solid line). Values of AGB/AGB$_{initial}$ > 1 represent seagrass growth potential and below 1 indicate potential seagrass decline at day 14 of the simulation.

5

10

15

20

25

20

1.2 Revised manuscript

Development of a Submerged Aquatic Vegetation Growth Model in a Coupled Wave-Current-Sediment Model (COAWST v3.4)

Tarandeep S. Kalra[1], Neil K. Ganju[2], and Jeremy M. Testa[3]

[1]Integrated Statistics, contracted to the U.S. Geological Survey, Woods Hole, MA 02543, USA
[2]U.S. Geological Survey, Woods Hole, MA 02543, USA
[3] University of Maryland Center for Environmental Science, Solomons, MD, 20688, USA

Correspondence to: Tarandeep S. Kalra (tkalra@contractor.usgs.gov)

0 Abstract

The coupled biophysical interactions between submerged aquatic vegetation (SAV), hydrodynamics (currents and waves), sediment dynamics, and nutrient cycling have long been of interest in estuarine environments. Recent observational studies have addressed feedbacks between SAV meadows and their role in modifying current velocity, sedimentation, and nutrient cycling. To represent these dynamic processes in a numerical model, the presence of SAV and its effect on hydrodynamics (currents and waves) and sediment dynamics was incorporated into the open source model COAWST. In this study, we extend the COAWST modelling framework to account for dynamic changes of SAV and associated epiphyte biomass. Modelled SAV biomass is represented as a function of temperature, light, and nutrient availability. The modelled SAV community exchanges nutrients, detritus, dissolved inorganic carbon, and dissolved oxygen with the water-column biogeochemistry model. The dynamic simulation of SAV biomass allows the plants to both respond to and cause changes in water column and sediment bed properties, hydrodynamics, and sediment transport (i.e., a two-way feedback). We demonstrate the behavior of these modelled processes through application to an idealized domain, then apply the model to a eutrophic harbour where SAV dieback is a result of anthropogenic nitrate loading and eutrophication. These cases demonstrate an advance in the deterministic modelling of coupled bio-physical processes and will further our understanding of future ecosystem change.

1 Introduction

Submerged aquatic vegetation (SAV), or seagrasses, are rooted vascular plants that inhabit sediments of estuaries and coastal waters, with a wide global distribution. SAV are important primary producers in shallow environments, provide habitat for a number of aquatic organisms, can slow water velocities and dampen wave energy to trap particulate material (Carr et al., 2004), and can alter biogeochemical cycles through oxygenation of sediments (Larkum et al., 2006). The positive impact of ecosystem services provided by SAV presence has been well-studied

21

(Hemminga and Duarte, 2000, Nixon et al., 2001, Terrados and Borum, 2004. and McGlathery et al., 2007, Hayn et al., 2014). The growth of SAV is dependent upon light availability at the leaf surface, which is a function of light attenuation in the water-column and the biomass of epiphytic algae growing on SAV stems. During the last several decades, the loss of SAV has accelerated owing to anthropogenic pressures (Kennish et al., 2016) or natural causes

5   such as storms (Hamberg et al., 2017). One of the dominant factors of SAV loss is eutrophication through nutrient loading, exemplified by increased phytoplankton growth and epiphytic growth on vegetation. This results in a reduction of light availability (Burkholder et al., 2007), causing a loss of SAV habitat (Cabello-Pasini et al., 2003, Short and Neckles, 1999).

        The complex interactions between light availability, nutrient loading, SAV dynamics, hydrodynamics, and
10   sediment transport can be investigated using numerical modelling tools. Few modelling efforts have attempted to couple the effects of hydrodynamics and light availability to model the growth of SAV. Everett et al., 2007 and Hipsey and Hamilton, 2008 coupled the effects of chlorophyll and water to account for SAV variability while Bissett et al., 1999a, 1999b used spectral underwater irradiance to model the light availability required for SAV growth. Carr et al., 2012a, 2012b developed a one-dimensional coupled hydrodynamics, sediment, and vegetation growth dynamics
15   model. The model solved for vertical 1-D dynamics of SAV growth through a change in biomass that depended on water temperature, irradiance and seagrass properties Ganju et al., 2012 used a three-dimensional circulation model (ROMS) coupled to a Nutrient Phytoplankton Zooplankton Detritus (NPZD) eutrophication (water column bio-geochemistry model) developed by Fennel et al., 2006 and integrated the spectral light attenuation formulation (bio-optical model) provided by Gallegos et al., 2011. These models were linked to a benthic seagrass model to calculate
20   seagrass distribution (Zimmerman et al., 2003) and applied on the temperate estuary of West Falmouth Harbor (del Barrio et al., 2014). While the model was able to capture the loss of SAV due to insufficient light, it did not include interactions with epiphytes or exchanges with water-column nutrient and gas pools. The hydrodynamic feedbacks (change in currents and waves) and morphodynamic changes (sediment distribution) due to presence of SAV were also ignored. While these dynamic processes have significant implications for coastal ecosystem resilience, numerical
25   models that allow for the two-way feedbacks between hydrodynamics, sediment transport, and SAV growth and nutrient cycling have generally been lacking.

        Recently, Beudin et al. 2017 implemented the physical effects of SAV in a vertically varying water column through momentum extraction, vertical mixing as well as accounting for wave dissipation due to vegetation. These
30   processes were implemented within the open source COAWST (Coupled-Ocean-Atmospheric-Wave-Sediment Transport) modelling system that couples the hydrodynamic model (ROMS), the wave model (SWAN) and the Community Sediment Transport Modelling System (CSTMS) (Warner et al., 2010). Through this effort, the COAWST framework accounted for the coupled seagrass-hydrodynamics interactions. The model reproduced the turbulent shear stress across the canopy interface and peaked at the top of the canopy similar to the observations of Ghisalberti and
35   Nepf (2004, 2006). The presence of seagrass patch led to a reduced shear-scale turbulence within the canopy and an enhanced wake-scale generated turbulence. For more details on the impact of seagrass on hydrodynamics, readers are referred to Beudin et al. 2017. The inclusion of the physical effects of SAV on flow and sediment dynamics (Beudin

et al., 2017) in COAWST allows us to develop a framework that results in dynamic growth of SAV using the temperature, nutrient loading and light availability in the water column. Therefore, in this work we implement a SAV growth model that dynamically changes the SAV properties (stem density and height). The growth of SAV is modeled as biomass which includes the above ground (stems and shoots), below ground (roots and rhizomes) biomass and epiphyte biomass. Individual biomass equations described in the implementation of SAV growth model (section 2.2) are based upon previous SAV biomass models (primarily Madden and Kemp 1996), some of which have been previously implemented to simulate growth conditions for SAV in three-dimensional numerical model simulations (e.g. Cerco and Moore 2001). The change in biomass leads to a spatial and temporal variation of SAV density and height. With the inclusion of the SAV growth model, SAV can grow or dieback while contributing and sequestering nutrients from the water column (modifying the biological environment), and subsequently affect the hydrodynamics and sediment transport (modifying the physical environment). Conversely, a change in the physical environment, for instance the amount of sediment in the water column, can decrease light availability, and cause SAV dieback leading to reduced wave attenuation, increased sediment resuspension, and a further decrease of light availability.

We demonstrate the two-way biophysical coupling framework as follows: the SAV growth model and integration into COAWST are discussed in section 2; in section 3, the model setup for the idealized domain and a realistic simulation of West Falmouth Harbor, MA are described; in section 4, we present the results from the two model configurations along with a discussion of limitations of the current modelling work and in section 5, we summarize our work and outline areas of future research.

2 **Methods**

2.1 **Inclusion of SAV effect on flow and sediment dynamics in the numerical model**

Beudin et al. (2017) implemented the parameterizations that accounted for the presence of SAV within a coupled hydrodynamic and wave model within the open-source COAWST numerical modelling system (Warner et al., 2008). The COAWST framework utilizes ROMS (Regional Ocean Modelling System) for hydrodynamics with a wave model - SWAN (Simulating WAves Nearshore) via the Model Coupling Toolkit (MCT) generating a single executable program (Warner et al., 2008). ROMS (Regional Ocean Modelling System) is a three-dimensional, free surface, finite-difference, terrain-following model that solves the Reynolds-Averaged Navier-Stokes equations using the hydrostatic and Boussinesq assumptions (Haidvogel et al., 2008). The transport of turbulent kinetic energy and generic length scale are computed with a generic (GLS) two-equation turbulence model. SWAN (Simulating WAves Nearshore) is a third-generation spectral wave model based on the action balance equation (Booij et al., 1999). In ROMS, the presence of SAV extracts momentum, adds wave-induced streaming, and generates turbulence dissipation. Similarly, the wave dissipation due to vegetation modifies the source term of the action balance equation in SWAN. All these sub-grid scale parameterizations account for changes due to vegetation in the water column extending from the bottom layer to the height of the vegetation. SWAN only accounts for wave dissipation due to vegetation at the bottom layer. The coupling between the two models occurs with an exchange of water level and depth averaged velocities from ROMS to SWAN and wave fields from SWAN to ROMS after a desired number of time steps. The vegetation properties are separately input in the two models at the beginning of the simulations. Through these

23

changes, the SAV can affect the bottom stress calculations that determine the resuspension and transport of sediment, providing a feedback loop between SAV-sediment dynamics-hydrodynamics and wave dynamics. To account for sediment dynamics, the Community Sediment Transport Modelling System (CSTMS) (Warner et al., 2010) is used to track the transport of suspended-sediment and bed load transport under the action of current and wave-current forcing.

5   The model can represent an unlimited number of user defined sediment classes.

2.2 SAV growth model

The SAV growth model is primarily based upon a previous growth model developed and implemented in Chesapeake Bay by Madden and Kemp (1996). The model simulates the temporal dynamics of above ground biomass

10   (AGB) that consists of stems or shoots, and the below ground biomass (BGB) that consists of roots or rhizomes. In addition to AGB and BGB, epiphytic algal biomass (EPB) is simulated to account for reductions in light availability to plant leaves due to shading of SAV leaves by epiphytes under high nutrient loading conditions. AGB, BGB and EPB are simulated as total biomass per unit area, with nitrogen as the currency for biomass. Changes in AGB and BGB pools are simulated as a function of primary production and respiration, mortality (e.g. grazing), and nitrogen

15   exchange through the seasonal translocation of nitrogen between roots and shoots. EPB are modelled as a function of primary production, respiration, and mortality.

The remaining section describes the source terms that calculate the evolution of AGB, BGB and EPB and denoted by α, β and γ respectively. Table 1 and Table 2 describe model variables and input parameters along with their equivalent symbols used in the source code.

20   2.1 Primary production (ρ_s): The primary production of α depends on the maximum potential growth rate (μ_s) and downward deviations from this maximal rate resulting from light (φ_s) and nutrient (ϑ_s) availability as:

$$\rho_s = \mu_s \min(\varphi_s, \vartheta_s) \tag{1}$$

The maximum potential growth (μ_s) can be described as:

$$\mu_s = \lambda_s \, \vartheta_s \, g_s \exp[r_s \left(\frac{1.0}{T - T_o}\right)] \tag{2}$$

25   where λ_s is a self-shading parameter that accounts for crowding and self-shading within the SAV canopy, g_s accounts for SAV's maximum growth fraction, r_s is the active SAV respiration coefficient, T is the temperature in water column, T_o is the user defined optimum temperature that allows for species specific sensitivities to temperature. The self-shading parameter, λ_s used in Eq. 3 is calculated by setting a maximum aerial biomass of SAV (Madden and Kemp 1996), thereby making growth rates density-dependent and is defined as:

30    $$\lambda_s = 1 - \left(\frac{\alpha}{\lambda_{s,max}}\right)^2 \tag{3}$$

where α is the above ground SAV biomass and $\lambda_{s,max}$ accounts for the maximal SAV biomass.

The availability of photosynthetically active radiation (PAR) represented by mathematical symbol θ for SAV leaves in the bottom cell is simulated using a bio-optical model (Gallegos et al. 2009, del Barrio et al. 2014). While the bio-

24

optical model generates predictions of light available across the spectrum within PAR, the light availability (φ_s) used to compute primary production (Eq. 1) is obtained through traditional photosynthesis-irradiance (PI) curves based on total PAR used to represent SAV growth responses to light:

$$\varphi_s = \frac{\theta}{l_s + \theta} \tag{4}$$

5 where l_s is the half-saturation for light limitation for SAV and θ refers to photosynthetically available radiation that is obtained from the bio-optical model. This simplified PI formulation, which has been applied in previous SAV models (Madden and Kemp 1996, Zaldívar et al. 2009, Jarvis et al. 2014) is applied so that a general and flexible SAV growth response is available for users in a wide-variety of environments with different species. More complex approaches can easily be applied (e.g. Zharova et al. 2001, Carr et al. 2012). The nutrient limitation (ϑ_s) required in

10 Eq.1 to compute primary production represents the fact that rooted plants can obtain nutrients from both sediments (as in Madden and Kemp, 1996) and the water-column and is defined as:

$$\vartheta_s = DIN_{wc} + \frac{n_{s,1} DIN_{sed}}{n_{s,2} DIN_{sed} + n_{s,1} DIN_{sed}} \tag{5}$$

where DIN_{wc} is the dissolved inorganic nitrogen concentration in the water column based on the sum of NH_4 (Ammonium) and NO_3 (Nitrate) in the water column and DIN_{sed} is the amount of dissolved inorganic nitrogen (DIN

15 $= NH_4 + NO_3$) in the sediment bed layer, and $n_{s,1}$ is the half-saturation for nutrient limitation for SAV roots.

2.2.2 Respiration: SAV respiration terms are partitioned into active and basal respiration, where the active respiration term represents respiration that is dependent on the photosynthesis rate, and the basal rate represents maintenance respiration rate. The active respiration term is defined as:

20 $$\delta_s = \rho_s \, p_s \exp(r_s \, T) \tag{6}$$

where ρ_s is the primary production term (Eq. 1), p_s is the maximum fraction of photosynthesis available for respiration, r_s is the SAV's active respiration coefficient, T is the temperature in the water column. The above ground basal respiration term is defined as:

$$\varepsilon_s = c_s \exp(h_s \, T) \tag{7}$$

25 where c_s is the maximum fraction of SAV below ground biomass (BGB) that is respired, h_s is the SAV basal respiration coefficient for both AGB and BGB, T is the temperature in the water column.

2.2.3 Mortality: The mortality of SAV is computed separately for above-ground and below-ground biomass, where above ground mortality ($\omega_{s,1}$) accounts for the sloughing of leaves and grazing in combination as:

$$\omega_{s,1} = (m_\alpha \, \alpha)^2 \tag{8}$$

30 where m_α is the above ground SAV mortality rate (sloughing).

Below ground mortality, $\omega_{s,2}$, is a function of temperature and is given as:

$$\omega_{s,2} = 0.01 \, \beta \exp(m_\beta \, T) \tag{9}$$

where m_β is the below-ground SAV mortality rate. Additional terms include that modify the AGB and BGB include

35 the seasonal exchange (translocation) of root material (nitrogen) quantified as a fraction of primary production and the translocation of BGB to AGB which represents the seasonal translocation of nitrogen from roots to stems as the

25

plants initially emerge in spring. Each of these terms is initiated on a specified day of the year (Madden and Kemp 1996), and can be altered to account for species differences or regional differences in the physiology of particular species. Translocation of nitrogen from leaves to roots/rhizomes (storage) is modelled as a continuous response to SAV primary production (ρ_s) and is given by defining $\sigma_{s,1}$ (translocation of above ground biomass to below ground biomass) as:

$$\sigma_{s,1} = \rho_s\, k_1 \tag{10}$$

where k_1 is a downward translocation coefficient.

and translocation from roots/rhizomes to leaves (upward translocation) is modelled as a simple linear function of below ground biomass (denoted by β) that begins after a user-defined threshold temperature is crossed and is given by defining $\sigma_{s,2}$ (translocation of below ground biomass to above ground biomass) as:

$$\sigma_{s,2} = \beta\, k_2 \tag{11}$$

where k_2 is a upward translocation coefficient.

The epiphyte biomass (EPB) is computed similarly to SAV biomass by simulating EPB as a function of primary production, respiration, and mortality (e.g. grazing).

2.2.4 Primary production (ρ_e): The primary production of EPB depends on the maximum potential growth rate (μ_e) and a limitation between light (φ_e) and nutrient (ϑ_e) availability, as:

$$\rho_e = \mu_e\, \min(\varphi_e, \vartheta_e) \tag{12}$$

The maximum potential growth of EPB (μ_e) can be described as:

$$\mu_e = \lambda_e\, \vartheta_e\, g_e\, \exp\!\left[r_e\left(\frac{1.0}{T - T_{e,o}}\right)\right] \tag{13}$$

where λ_e is the self-shading parameter that accounts for spatial limits on the epiphyte population, g_e accounts for epiphyte's maximum growth fraction, r_e is the active epiphyte respiration coefficient, T is the temperature in water column, $T_{e,o}$ is the user defined optimum temperature that allows for species-specific sensitivities to temperature. λ_e is calculated by setting a maximum aerial biomass of EPB, thereby making growth rates density-dependent similar to the SAV growth rate, as:

$$\lambda_e = 1 - \left(\frac{EPB}{\lambda_{e,max}}\right)^2 \tag{14}$$

where EPB is the epiphyte biomass and $\lambda_{e,max}$ is the maximum epiphyte biomass.

The light availability (φ_e) used to compute primary production (Eq. 10) is obtained through traditional photosynthesis-irradiance (PI) curves used to represent epiphyte growth response to light, as:

$$\varphi_e = \frac{\theta}{l_e + \theta} \tag{15}$$

where l_e is the half-saturation for light limitation for epiphytes and θ is the photosynthetically available radiation obtained from the bio-optical model. The nutrient limitation (ϑ_e) required in Eq.1 to compute primary production for

epiphytes depends only on the nutrients in the water-column and is a traditional algal form (e.g. Monod model) given as:

$$\vartheta_e = \frac{n_e \, DIN_{wc}}{n_e \, DIN_{wc} + n_e} \tag{16}$$

where DIN_{wc} is the amount of dissolved inorganic nitrogen in the water column, n_e is the half-saturation for nutrient
5   limitation for epiphytes.

2.2.5 Respiration: Epiphyte respiration terms are partitioned into active and basal respiration, where the active respiration term represents respiration that is dependent on the photosynthesis rate, the basal rate represents the maintenance respiration rate. The active respiration term is defined as:

10     $$\varepsilon_{e,1} = \rho_e \, p_e \exp(r_e \, T) \tag{17}$$

where ρ_e is the primary production term (Eq. 1), p_e is the maximum fraction of photosynthesis for epiphytes, r_e is the epiphyte's active respiration coefficient, T is the temperature in the water column.

The basal respiration term is defined as:

$$\varepsilon_{e,2} = c_e \exp(h_e \, T) \tag{18}$$

15

2.2.6 Mortality: The mortality of epiphytes depends on mortality and grazing of algal cells, as well as losses associated with SAV sloughing (which effectively removes epiphytes from a cell). The mortality term is given as a simple linear form:

$$\omega_e = m_e \, \gamma \tag{19}$$

20   where m_e is the epiphyte mortality rate. The loss of epiphyte biomass due to grazing ($\tau_{e,1}$) modelled using an Ivlev function can be described as:

$$\tau_{e,1} = z_{e,max} \, [1.0 - \exp(-z_e)] \tag{20}$$

where $z_{e,max}$ is the maximum grazing rate on epiphytes and z_e is the grazing coefficient on epiphytes. The reduction of epiphyte biomass due to the SAV sloughing loss is computed as:

25     $$\tau_{e,2} = \left(\frac{\omega_{s,1} \, t}{\alpha}\right) \tag{21}$$

where $\omega_{s,1}$ is the above ground mortality term described in Eq. 8, is the time step size in per day units and α refers to the above ground biomass.

The above ground biomass (AGB) computed in the SAV growth model is utilized to obtain SAV shoot height (meters)
30   and stem density (stems/m^2), to allow for the biomass model (AGB) to be translated into variables input into the SAV-hydrodynamic coupling. The shoot height (l_v) is related to AGB (denoted by α) as:

$$l_v = 0.45 \left(\frac{\alpha}{120.0 + \alpha}\right) \tag{22}$$

The relationship is based on measurements of *Zostera marina* in Chincoteague Bay and Chesapeake Bay (Fig. 2), but is consistent with relationships for *Z. marina* determined elsewhere (Krause-Jensen et al., 2000). Other three-
35   dimensional models have used similar formulations (e.g. Cerco and Moore, 2001 for Chesapeake Bay). SAV stem

27

density n_v, (in stems/m^2) is computed from a similar empirical formulation based on relationships in Krause-Jensen et al., 2000 and is computed as:

$$n_v = 4.45\,\alpha \tag{23}$$

2.3 Integration of SAV growth model with Water-Column Biogeochemistry Model (BGCM model)

The SAV growth model is built to interact dynamically with the water-column biogeochemistry model (BGCM model) within the COAWST modelling framework. We utilize one of the existing BGCM models developed by Fennel et al., 2006 that accounts for nutrients (NO_3, NH_4), phytoplankton and zooplankton biomass, and detritus. The BGCM model in the current simulations solved for twelve state variables. The spectral irradiance model that provides the light attenuation in response to chlorophyll, sediment, and CDOM was previously integrated (Gallegos et al. 2009, del Barrio et al. 2014) into the BGCM model. The BGCM model was implemented within the hydrodynamic component of COAWST model, ROMS (Regional Ocean Modeling System). ROMS is a three-dimensional, free surface, terrain-following numerical model that solves finite-difference approximations of the RANS equations using the hydrostatic and Boussinesq assumptions (Chassignet et al., 2000 and Haidvogel et al., 2000). ROMS is discretized in horizontal dimensions with curvilinear orthogonal Arakawa C grid (Arakawa, 1966). Each state variable is calculated based on the tracer transport equation with tracer concentrations calculated at the grid cell centers as follows:

$$\frac{\partial c}{\partial t} + u\frac{\partial c}{\partial x} + v\frac{\partial c}{\partial y} + w_d\frac{\partial c}{\partial z} = \frac{\partial}{\partial z}\left(v\frac{\partial c}{\partial z}\right) + C_{source} \tag{24}$$

where C is the tracer quantity, t is time, x and y are the horizontal coordinates and z is the vertical coordinates. u and v are the horizontal components of current velocity with w_d being the sinking velocity for tracers such as detritus. v is the turbulent diffusivity coefficient and C_{source} is the tracer source/sink term, which represents the net effects of all sources and sinks in this representation. There are several choices of advection schemes for tracer advection available in COAWST (Kalra et al., 2019) and in the current simulations, we utilized Multidimensional Positive Definite Advection Transport Algorithm (MPDATA) scheme (Smolarkiewicz, 1984) that has been derived from Lax Wendroff (LW) family of schemes. The time marching scheme for tracers involves a predictor-corrector step using the leapfrog-trapezoidal methods. The 3-D tracer equations are solved at a different and shorter time step than the depth-integrated 2-D barotropic equations. The integration between the baroclinic mode and barotropic mode is performed using a split-explicit time step approach (Shchepetkin and McWilliams, 2005, 2009). The predictor step calculates the tracer values that updates the momentum equations at an intermediate time step. At that point, the split-explicit algorithm is executed and the update of tracers is done using the corrector step after the new values of velocity are available. For more details of this algorithm, readers are readers are referred to Shchepetkin and McWilliams, 2005 and 2009. The vertical tracer diffusion terms are solved using a fourth-order centered scheme (Shchepetkin and McWilliams, 2005). The vertical advective fluxes are computed using the piecewise parabolic method (Colella and Woodward, 1984). The vertical terms utilize a backwards Euler method for time marching.

28

The changes in water-column variables (dissolved and particulate nitrogen, dissolved oxygen, dissolved inorganic carbon) due to the SAV growth model occur locally at the bottom cell through the source terms (C_{source}) that affect six state variables in the BGCM model: NO_3 (Nitrate), NH_4 (Ammonium), DO (Dissolved Oxygen), CO_2 (Carbon dioxide), $LDeN$ (Labile Detrital Nitrogen), $LDeC$ (Labile Detrital Carbon). The change in these state variables based on the SAV growth model is as follows:

$$\frac{\partial DIN_{SAV}}{\partial t} = (\delta_s + \varepsilon_s - \rho_s)(1 - s_f)t + (\varepsilon_{e,1} + \varepsilon_{e,2} - \rho_e)t \tag{25}$$

where $\frac{\partial DIN_{SAV}}{\partial t}$ is the net impact of SAV and epiphyte growth on water-column nitrogen concentrations and s_f decides the portioning of nutrient uptake between sediment and water column using a logistic function and is defined as:

$$s_f = 1 - \left(\frac{1}{1+\exp[-m_f(DIN_{wc}-k_f)]}\right) \tag{26}$$

where m_f and k_f are constants and equal to 0.2 and 15.0 respectively and DIN_{wc} (Dissolved Inorganic Nitrogen) is calculated as a sum of state variables NH_4 (Ammonium) and NO_3 (Nitrate) in the water column. If net growth from SAV and epiphytes is negative, the net nitrogen regeneration is realized as NH_4 production in the water column ($\frac{\partial NH_4}{\partial t} = \frac{\partial DIN_{SAV}}{\partial t}$). If there is net growth originating from SAV and epiphytes, the associated water column uptake of DIN is apportioned between NO_3 and NH_4 relative to their availability in the water-column via the following equations:

$$\frac{\partial NH_4}{\partial t} = \left(\frac{\partial DIN_{SAV}}{\partial t}\right)\left(\frac{NH_4}{DIN_{wc}}\right) \tag{27}$$

$$\frac{\partial NO_3}{\partial t} = \left(\frac{\partial DIN_{SAV}}{\partial t}\right)\left(\frac{NO_3}{DIN_{wc}}\right) \tag{28}$$

$$\frac{\partial DO}{\partial t} = \left(\rho_s - \delta_s - \varepsilon_s + \rho_e - \varepsilon_{e,1} - \varepsilon_{e,2}\right)t \tag{29}$$

$$\frac{\partial CO_2}{\partial t} = \left(\delta_s + \varepsilon_s - \rho_s + \varepsilon_{e,1} + \varepsilon_{e,2} - \rho_e\right)t \tag{30}$$

$$\frac{\partial LDeN}{\partial t} = \left(\omega_{s,1} + \omega_e + \tau_{e,1}\right)t \tag{31}$$

$$\frac{\partial LDeC}{\partial t} = \left(\omega_{s,1} + \omega_e + \tau_{e,1}\right)t \tag{32}$$

All the source terms in equations (25 and 27-32) are solved using the SAV growth model described in Section 2.2 and in equation 30 and 32, these terms are converted to moles of Carbon from moles of Nitrogen assuming a fixed (and user-defined based on local data) C:N ratio in SAV tissue (we assumed a C:N of 30).

2.4 Two-way feedback from SAV to hydrodynamics, waves, sediment dynamics, and biogeochemistry

29

The addition of the SAV growth model leads to the biological evolution of SAV properties based on temperature, light, and nutrient availability. The modelled SAV community exchanges nutrients. detritus, dissolved oxygen, and dissolved inorganic carbon with the water-column BGCM. Changes in SAV biomass, and canopy characteristics also impacts hydrodynamics, wave dynamics and sedimentary dynamics (resuspension-transport). By lowering the current

5 speed and attenuation of wave flow, the reduction in bed shear stresses in the vegetation canopy reduces sediment resuspension; thereby altering sediment transport in the model (as described in Section 2.1), that feedback to control light availability and, in turn, potential seagrass biomass production. This methodology of including the SAV growth model enables the COAWST framework to have a two-way feedback between hydrodynamic-biological coupling. Figure 1 describes the coupling process between different modules schematically.

10

3. Model Setup

3.1 Idealized test case

The implementation of the SAV growth model within the COAWST framework is first tested on an idealized domain. The test case consists of an idealized rectangular domain of 9.2 km width and 9.8 km length with a 1 m deep

15 basin. The number of interior domain points are 90 in the x-direction and 98 in the y-direction with 10 vertical sigma layers. The resulting domain has a grid resolution of 100 m by 100 m in horizontal and 0.1 m in the vertical (this varies with water level). A rectangular vegetation bed extends from the north boundary of the domain southward 8 km, with a width of 1.8 km, centered in the domain (Figure 3). The ROMS barotropic and baroclinic time steps are 0.05 s and 1 s respectively. The bed roughness is set to z_o =1.5 mm. The k − ε turbulence model is implemented following the

20 GLS method (Warner et al., 2005). The initial AGB, BGB and EPB in the vegetation bed are set to be 90, 15 and 0.01 mmol N/m^2 respectively. The vegetation density, height, diameter and thickness are initialized to be 400 stems/m^2, 0.19 m, 1.0 mm and 0.1 mm respectively. The vegetative drag coefficient (C$_D$) is set to be 1 (typical value for a cylinder at high Reynolds number). The imposed surface wind speed is 3 m/s from the north to induce a wave field. The surface air pressure is initialized as 101.3 kPa. The kinematic surface solar shortwave radiation is set to an

25 amplitude of 500.0 W/m^2 with a 24-hour period. The kinematic surface longwave radiation flux is set to zero (W/m^2). The surface air temperature varies between 1.5 ℃ to 18.5 ℃ over a yearly period. The surface solar downwelling spectral irradiance just beneath the sea surface is set following Gregg and Carder (1990). The cloud fraction is set to be zero. The bulk flux parameterizations in COAWST for surface wind stress and surface heat flux are based on the COARE code (Fairall et al. (1996a, 1996b) and Liu et al. (1979)).

30 The model is forced by oscillating the water level on the northern boundary with a tidal amplitude of 0.25 m and a period of 12 hours. Northern boundary conditions include a water temperature variation between 1.5 ℃ to 18.5℃ over an yearly period. Salinity and NO_3 at the northern boundary are set to 35 psu and 20 mmol N/m^3 respectively, and we impose a suspended sediment concentration of 0.5 g/L as well. The northern boundary condition for tracers is a radiation condition with nudging on a 6h timescale. For both flow and tracer fields (physical and biological), the

35 western and eastern boundaries have a gradient condition and the southern boundary is closed. The model setup for the idealized domain is simulated for 60 days and the model output is averaged over each day.

3.2 Realistic test case: West Falmouth Harbor, Massachusetts, USA

del Barrio et al. (2014) used an offline coupling of the COAWST model with a bio-optical seagrass model (Zimmerman et al., 2003) to study the influence of nitrate loading and sea-level rise on seagrass presence/absence in West Falmouth Harbor, Massachusetts, USA. Nitrate concentrations in groundwater exceeded 200 μM due to a

5 wastewater treatment plant in the watershed, however recent mitigation is expected to eliminate the nitrate load in the future. The model of del Barrio et al. (2014) used the biogeochemical results to generate spectral irradiance fields which were then passed to the bio-optical model. While useful for investigating the interaction between phytoplankton dynamics, light climate, and potential seagrass coverage, that model did not account for the interaction of seagrass with water column and sediment nitrogen pools, or hydrodynamics. Therefore, we tested the fully coupled

10 hydrodynamic, biogeochemical, and vegetation model using the same hydrodynamic and biogeochemical model setup (Ganju et al., 2012 and del Barrio et al., 2014), but with the full vegetative interaction implemented. Briefly, the model is forced with tides at the western boundary, groundwater and nitrate loading at the eastern boundary, and solar irradiance at the air-sea boundary. Further details on the model setup are given by Ganju et al. (2012) and del Barrio et al. (2014). The hydrodynamic and biogeochemical (e.g. chlorophyll concentrations, light attenuation) results were

15 assessed in those studies. In this work, we test the ability of the coupled model to reproduce the present-day spatial pattern of seagrass presence, with growth and persistence expected in the outer harbor, and dieback in the inner harbor, where nitrate loading, phytoplankton growth, and light attenuation are highest. The initial SAV properties include a plant height of 0.195 m, plant density of 110 stems/m^2, plant diameter of 0.001 m, and plant thickness of 0.0001 m. The vegetative drag coefficients C_D in the flow model and the wave model are set to 1 (typical value for a cylinder at

20 high Reynolds number). We utilize the SAV growth model parameters described in Table 1. The model setup for West Falmouth Harbor (Section 3.2) is simulated for 56 days, beginning 2 July 2010 (Ganju et al., 2012).

4 Results and Discussion

4.1 SAV, sediment, and hydrodynamics in the idealized test case

25 Simulations of the coupled hydrodynamic-biogeochemical-SAV model revealed the integrated nature of estuarine dynamics in response to submerged macrophytes. In these simulations, SSC was imposed at the northern open boundary at concentrations of 0.5 g/L (and zero g/L within the bed), resulting in a decline in SSC as one moves towards the southern boundary (Fig. 4a). This distribution of SSC input results in an increase in light attenuation (K_{dpar}=30.0 m^{-1}) in the region close to the northern boundary (0.0 km), while background conditions prevail in the

30 southern reaches (Fig. 4b). In Fig. 4b, SSC input from the northern boundary causes a decrease in light availability within the modelled SAV region between the open boundary in the north and about 2.4 km into the SAV bed. Consequently, these sub-optimal light conditions in the northern 2.4 km of the SAV bed cause AGB to decrease from its initial value of 90.0 millimoles N/m^2 to 30.0 millimoles millimoles/m^2 (Fig. 5a). Boundary effects associated with SSC inputs are substantially muted in the region between 2.4 km and 8.0 km within the SAV bed (Figs. 4&5), where

35 in-bed SSC concentrations are much lower than those outside the bed at the same distance from the boundary. As a consequence, where AGB biomass increases from its initial value of 90.0 millimoles N/m^2 to 150.0 millimoles N/m^2 over the course of the simulation. Increases in SAV biomass within the bed during the simulation led to increases in

SAV density and height, where SAV density increased from its initial value of 400 stems/m^2 to of 810 stems/m^2 owing to favourable light conditions from y=2.4 km to y=8.0 km. Thus, the model captured the role of SAV in resisting SSC transport into the bed, allowing for greater light availability and an increase in growth rates and biomass accumulation.

The temporal evolution of SAV biomass in response to the SSC input at the northern boundary further emphasizes the self-stimulating role of SAV in the idealized simulations. A comparison of model simulations at two locations within the initially described SAV bed of the idealized domain (indicated in Fig. 5a and corresponding to y=0.1 km and y=4.5 km from the northern boundary) reveal that close to the northern boundary (y=0.1 km), the daily averaged light attenuation remains high (above 30 m^{-1}) over the 60-day period (Fig. 5a). At y=0.1 km, the increased light attenuation in the northern location corresponds to the lack of light availability and this causes a decay of AGB from its initial value of 90.0 millimoles N/m^2 to 30.0 millimoles N/m^2. (Fig. 5b). This decay in AGB over the 60-day period at y=0.1 km (SAV dieback), contrasts sharply with the AGB increases inside the SAV bed at the southern location (y=4.5 km), where light attenuation is lower because sediments have not penetrated the SAV bed, allowing for higher SAV growth rates. The higher SAV growth rate inside the SAV bed at y=4.5 km can be observed (Fig. 5c) by looking at the net primary production of SAV ($\rho_s - \delta_s - \varepsilon_s$). At this location (y=4.5 km), the SAV growth rate increases over the 60-day period while it keeps decreasing in the northern location (y=0.1 km). Due to the higher SAV growth inside the SAV bed (y=4.5 km), the SSC in the bottom cell remains low (Fig. 5d) and at y=0.1 km due to the SAV dieback, the sediment concentration in the water column stays high and above 0.25 g/L.

As mentioned above, the SSC input on the northern boundary of the idealized domain causes a region of sub-optimal light conditions that lead to the SAV dieback; while the SAV growth occurs in the remaining bed where favourable light conditions exist. The effect of change in SAV density and height on the hydrodynamics and morphodynamics at the end of the simulation can be demonstrated by using the same idealized domain. To this end, two transects are chosen that are along the length of the SAV bed and extend from the northern boundary towards the southern boundary. The transects are chosen inside at x=1.8 km (outside of the SAV bed) and at x=4.8 km (inside of the SAV bed). The depth-integrated SSC and bottom stresses averaged on the 60th day in the transect (Fig. 7a) outside of the SAV bed show that the profile of bottom stress follows the distribution of SSC along the transect. In Fig. 7a, a 0.2 N/m^2 of peak bottom stress is obtained at x=1.8 km (outside of the SAV bed) that corresponds to a depth-averaged SSC of 0.31 g/L. On the other hand, the transect within the SAV bed (Fig. 7b) shows that the region where SAV dieback has occurred (between 0.0 km to 2.4 km) corresponds to increased bottom stresses (0.13 N/m^2 at the north most location and a corresponding SSC of 0.26 g/L) while the region where the SAV growth has occurred, the bottom stresses are close to zero (i.e. from 2.4 km and onwards).

The simulation of the idealized domain demonstrates the capability of the modelling framework to perform two-way feedbacks between hydrodynamics, sediment and biological dynamics. The SSC input in the northern boundary affects the light attenuation in the domain and causes SAV dieback close to the northern boundary. The SAV grows in the region where favourable light conditions exist. The SAV dieback leads to increased bottom stresses while the growth of SAV leads to a decrease in bottom stresses; illustrating the fact that the SAV act as bottom sediment stabilizers by reducing SSC.

4.2 SAV growth in West Falmouth Harbor

The present-day simulation of seagrass dynamics reproduces the patterns of chlorophyll (via phytoplankton), light attenuation, and near-bottom PAR simulated by del Barrio et al., 2014. Nitrate loading from shoreline point sources led to increased phytoplankton growth indicated by increased chlorophyll and light attenuation in the landward,
5 northeast portion of the harbor (Fig. 8a,b), while bathymetric controls in the deeper central basin led to decreased near-bottom PAR (Fig. 8c). Peak AGB exceeds 100 millimoles N m^{-2}, while seagrass presence begins towards decline in the inner harbor and in the central basin as expected. Intertidal areas around the periphery of the harbor are devoid of AGB due to the enforced masking of areas with intermittent wetting and drying.

Time-series of these parameters (Fig. 9) from selected outer and inner harbor locations over the first 22 days
10 demonstrate the diurnal variability, as well as the rapid loss of AGB in the inner harbor due to the local nitrate loading, phytoplankton proliferation, and degraded light climate. The sizeable diurnal variability in AGB (Fig. 9d) appears to be an artifact of production/respiration formulations that are based on seasonal responses to environmental forcing, rather than diurnal responses to solar irradiance. Future modifications could attenuate this variability by utilizing daily averaged environmental forcing, or modifying the frequency of biomass updating.

15 The modelling framework developed in this work can be used to create hypothetical scenarios to estimate future environmental responses. For example, we ran the model setup of West Falmouth Harbor described in section 3.2 with no nitrate loading, to simulate a hypothetical scenario where the groundwater input has no influence from the wastewater treatment plant (unimpacted past or future scenario). The elimination of nitrate loading results in negligible changes in the outer harbor, but greatly reduces chlorophyll and light attenuation in the inner harbor (Fig. 10a,b), while
20 increasing the near-bottom PAR (Fig. 10c). Peak AGB responds to the decreased chlorophyll and increased light attenuation with an increase in the inner harbor (Fig. 10d). This implementation represents an incremental improvement to the prior modelling exercise (Ganju et al., 2012 and del Barrio et al., 2014), because the interaction between SAV and the nitrogen pools are explicitly accounted for. For example, this model can now be used to test how changes in seagrass coverage influence nitrogen retention within the estuary, or export to the coastal ocean.
25 Further, the introduction of seagrass kinetics will allow for investigation of water column oxygen budgets with and without seagrass, under present and future scenarios.

4.3. Model evaluation in West Falmouth Harbor

30 In order to qualitatively evaluate the seagrass growth model, we have compared the modeled results with observations by del Barrio et al. (2014) that measured the extent of seagrass coverage in West Falmouth Harbor (red outline in Fig. 11). The field data is only available for the northern region of WFH where the model-data comparisons are performed. The model results are compared by extracting the peak above ground biomass (AGB) on 14th day of the simulation and normalized with the initial above ground biomass. The ratio of AGB/AGB$_{initial}$ is considered as a representative
35 of seagrass growth. We assume that for AGB/AGB$_{initial}$ > 1, there is a potential for seagrass growth and for AGB/AGB$_{initial}$ <1, the conditions are unfavorable for seagrass growth. In fig 11, the model and field data show a 89% agreement to determine the seagrass growth or dieback. The western region of outer harbor shows seagrass growth potential and agrees with the extent that the seagrass coverage is observed. In the eastern region, the field data shows

33

no seagrass coverage and the model also predicts potential seagrass dieback. The model predicts seagrass dieback because of nitrate loading from shoreline point sources that leads to increased chlorophyll and light attenuation (figures 8a, b). The model and observations do not compare well in the central basin of outer harbor where the model shows seagrass dieback potential while the field data shows presence of seagrass. In the central basin, the field data shows the presence of seagrass while its density remains low in this region. On the other hand, the modelled seagrass suffers dieback due to the bathymetric controls in the deeper central basin (decreased near-bottom PAR Fig. 8c).

Direct estimates of above ground SAV biomass have also been recently made in West Falmouth Harbor (Hayn et al., unpublished data). Although these measurements were not made during the same year as our simulations (measurements in 2006, 2007, 2013; model 2010), the mean above ground biomass measured in the outer harbor of 49.5 (June 21-July 6 2006), 45.3 (June 6-19 2007), and 41.5 g C m^{-2} (July 15-19 2013) is consistent with the range of model simulations during a comparable period (July 2-19) in the outer (28.1 to 51.1 g C m^{-2}) and middle (14.9 to 37.4 g C m^{-2}) harbors. The July 2-19 model range of 45.7 to 156.3 mmol N m^{-2} across the middle and outer harbor is also consistent with annual mean *Z. marina* biomass (10-88 mmol N m^{-2}) reported in nearby shallow systems on Cape Cod (Hauxwell et al. 2003) assuming a literature-based average that above ground SAV biomass is 1.5% N. The range in the model is computed based on the minimum and maximum values of AGB during the 18 day simulation period.

4.4 Limitations of SAV growth model and Future Work

While this modelling approach represents an advance in modelling coupled biophysical processes in estuaries, there are limitations that must be addressed in future work:

1. The modelling of SAV dieback/growth scenarios may require long-term simulations on decadal timescales (Carr et al., 2018). However, the short model time step limits the duration of such simulations. The time step size is of the order of seconds (typical of 3-D ocean models) and this combined with the fact that the presence of SAV in the hydrodynamic model further limits time step size (due to hydrodynamic stability constraints); overall limits the applicability of the model to be utilized from monthly to annual time scales at this juncture.

2. The biomass equations described in Section 2.3 are formulated for seasonal time scales and are being used in the model implementation at every ocean model time step. This leads to large daily variations in above and below ground biomass that do not likely occur in the environment, although diel variations on SAV growth have been measured in situ (Kemp et al. 1987). Hence, with the current formulations, the output from the biomass model needs to be analyzed as a daily averaged quantity.

3. The current implementation of the SAV growth model is limited to only one SAV species. However, it should be extended to include multiple SAV species to investigate competition under variable salinity and to make the model applicable to a wider variety of locations.

5 Conclusions

The present study adds to the open source COAWST modelling framework by implementing a SAV growth model. Based on the change in SAV biomass (above ground, below ground) and epiphyte biomass, SAV density and height evolve in time and space and directly couple to three-dimensional water-column biogeochemical,

34

hydrodynamic, and sediment transport models. SAV biomass is computed from temperature, nutrient loading and light predictions obtained from coupled hydrodynamics (temperature), bio-geochemistry (nutrients) and bio-optical (light) models. In exchange, the growth of SAV sequesters or contributes nutrients from the water column and sediment layers. The presence of SAV modulates current and wave attenuation and consequently affects modelled sediment transport and fate. The resulting modelling framework provides a two-way coupled SAV-biogeochemistry-hydrodynamic and morphodynamic model. This allows for the simulation of the dynamic growth and mortality of SAV in coastal environments in response to changes in light and nutrient availability, including SAV impacts on sediment transport and nutrient, carbon, and oxygen cycling. The implementation of the model is successfully tested in an idealized domain where the introduction of sediment in the water column (SSC) at one end of the domain provides sub-optimal light conditions that causes SAV dieback in that region. The model was applied to the temperate estuary of West Falmouth Harbor, where simulations show the coupled effect of enhanced nitrate loading in the inner harbour leading to poor light conditions for the SAV to grow; thus modelling the physical effect of eutrophication leading to the loss of SAV habitat. Among other applications, in future, the model will be used assess the effects of sea level rise scenarios that limit light availability and potentially cause the loss of SAV habitat.

6 Code availability

The implementation of the SAV growth model has been implemented in the Coupled Ocean Atmosphere Waves Sediment-Transport Modeling System (COAWST v3.4). This particular version is available for download at: https://www.sciencebase.gov/catalog/item/5f15d69082cef313ed81996a. Users are encouraged to download COAWST

5 distributed through the USGS code archival repository. It is available for download on https://code.usgs.gov/coawstmodel/COAWST. The COAWST distribution files contain source code derived from ROMS, SWAN, WRF, MCT and SCRIP, along with the Matlab code, examples and a User's Manual.

The major code development that was done for this project is contained within the COAWST folder on the following path. "https://code.usgs.gov/coawstmodel/COAWST/blob/master/ROMS/Nonlinear/Biology/"

10 This folder contains several methods of computing water column biogeochemistry. Other than the I/O component of our implementation, the algorithmic development in this study only modifies two files on this path: "estuarybgc.h" and "sav_biomass.h". The file "sav_biomass.h" contains all the newly added equations for the growth of SAV based on the nutrient loading in the water column. The forcings to the SAV growth model (temperature, light, nutrient availability, exchanges nutrients, detritus, dissolved inorganic carbon, and dissolved oxygen) are provided through the file "estuarybgc.h" that calls

15 "sav_biomass.h". The file "estuarybgc.h" solves for the water column biogeochemistry and was based on existing modelling framework developed by Fennel et al. (2006) (also coded as "fennel.h").

Other important paths that existed in the framework prior to the current modeling effort but are being used in the modeling process include:

1. "https://code.usgs.gov/coawstmodel/COAWST/blob/master/ROMS/Nonlinear"-

20 The main kernel of the 3-D non-linear Navier-Stokes equations is contained within this part and links all the submodels: biological, vegetation and sediment models.

2. "https://code.usgs.gov/coawstmodel/COAWST/blob/master/ROMS/Nonlinear/Vegetation/"

The kernals that account for seagrass-hydrodynamics interactions.

3. "https://code.usgs.gov/coawstmodel/COAWST/blob/master/ROMS/Nonlinear/Sediment/"

25 The kernals that account for sediment transport.

7 Data availability

The model data was released as per the USGS model data release policy and separate digital object identifiers were created as part of the release (https://www.usgs.gov/products/data-and-tools/data-management/data-release). The model output can be

30 accessed through sciencebase entries for the idealized test case simulation (Kalra and Ganju, 2019) and West Falmouth Harbor simulations (Ganju and Kalra, 2019).

8 Author contribution

T. S. Kalra implemented the SAV growth model in the COAWST framework. J. Testa provided guidance on the mechanistic processes affecting the growth of SAV from biomass parameterizations and developed linkages between the SAV growth model and the water-column biogeochemical model. N. K. Ganju developed the test case and the realistic domain case. T. S. Kalra and N. K. Ganju performed the data analysis from the output of the test cases and were responsible for model data release. The manuscript was prepared with contributions from all co-authors.

9 Disclaimer

This draft manuscript is distributed solely for purposes of scientific peer review. Its content is deliberative and pre-decisional, so it must not be disclosed or released by reviewers. Because the manuscript has not yet been approved for publication by the U.S. Geological Survey (USGS), it does not represent any official USGS finding or policy. Any use of trade, firm, or product names is for descriptive purposes only and does not imply endorsement by the U.S. Government.

11 References

Beudin, A., Kalra, T. S., Ganju, N., K., and Warner, J.C.: Development of a Coupled Wave-Current-Vegetation Interaction, Computers & Geosciences, 100, 76-86, 2017.

Bissett, W.P., Carder, K.L., Walsh, J.J., Dieterle, D.A.: Carbon cycling in the upper waters of the Sargasso Sea: II. Numerical simulation of apparent and inherent optical properties, Deep-Sea Research Part 1: Oceanographic Research Papers, 46, 271-317, 1999.

Burkholder, J.M., Tomasko, D.A., Touchette, B.W.: Seagrasses and eutrophication, Journal of Experimental Marine Biology and Ecology, 350, 46-72, 2007.

Booij N., Ris, R.C., and Holthuijsen, L.H.: A third-generation wave model for coastal regions, Part I, Model description and validation, Journal of Geophysical Research C4, 104, 7649-7666, 1999.

Cabello-Pasini, A., Muniz-Salazar, R., Ward, D.H.: Annual variations of biomass and photosynthesis in Zostera marina at its southern end of distribution in the North Pacific, Aquatic Botany, 76, 31-47, 2003.

Carr, J., D'Odorico, P., McGlathery, K., Wiberg, P.: Stability and bistability of seagrass ecosystems in shallow coastal lagoons: role of feedbacks with sediment resuspension and light attenuation, Journal of Geophysical Research, 115, G03011, 2010.

5 Carr, J. A., P. D'Odorico, P., McGlathery, K.J., and Wiberg, P.L.: Stability and resilience of seagrass meadows to seasonal and interannual dynamics and environmental stress, Journal of Geophysical Research, 117, G01007, 2012.

Carr, J. A., P. D'Odorico, P., McGlathery, K.J., and Wiberg, P.L.: Modeling the effects of climate change on eelgrass stability and resilience: future scenarios and leading indicators of collapse, Marine Ecology Progress Series, 448, 289-301, 2012.

10 Carr, J., Mariotti, G., Fahgerazzi, S. McGlathery, K.,and Wiberg, P.: Exploring the Impacts of Seagrass on Coupled Marsh-Tidal Flat Morphodynamics. Frontiers of Environmental Science, 6, 92, 2018.

Cerco, C.F. and Moore, K.: System-wide submerged aquatic vegetation model for Chesapeake Bay, Estuaries, 24, 522-534, 2001.

Chassignet, E.P., Arango, H.G., Dietrich, D., Ezer, T., Ghil, M., Haidvogel, D.B., Ma, C.-C., Mehra, A.,

15 Paiva, A.M., Sirkes, Z. Dynamics of Atmospheres and Oceans 2000, Vol. 32, pp. 155-183.

Cossarini, G., Querin, S., Solidoro, C., Sannino, G., Lazzari, P., Biagio, V. and Bolzon, G., Development of BFMCOUPLER (v1.0), the coupling scheme that links the MITgcm and BFM models for ocean biogeochemistry simulations, Geosci. Model Dev., 10, 1423–1445, https://doi.org/10.5194/gmd-10-1423-2017, 2017

Costello, C.T. and Kenworthy, W.J., Twelve-Year Mapping and Change Analysis of Eelgrass (Zostera marina)

20 Areal Abundance in Massachusetts (USA) Identifies Statewide Declines, Estuaries and Coasts, Vol, 34:232–242, 2011.

del Barrio, P., Ganju, N. K., Aretxabaleta, A. L., Hayn, M., García, A., and Howarth, R. W.: Modeling future scenarios of light attenuation and potential seagrass success in a eutrophic estuary, Estuarine, Coastal and Shelf Science, 149, 13-23, 2014.

Everett, J.D., Baird, M.E., Suthers, I.M.: Nutrient and plankton dynamics in an intermittently closed/open lagoon, Smiths Lake,

25 south-eastern Australia: an ecological model, Estuarine, Coastal and Shelf Science, 72, 690-702, 2007.

Fairall, C.W., Bradley, E.F., Rogers, D.P., Edson J.B., and Young, G.S.: Bulk parameterization of air-sea fluxes for tropical ocean global atmosphere Coupled-Ocean Atmosphere Response Experiment, Journal of Geophysical Research, 101, 3747-3764, 1996a.

Fairall, C.W., Bradley, E.F., Godfrey, J.S., Wick, G.A., Edson, J.B., and Young, G.S.: Cool-skin and warm-layer

30 effects on sea surface temperature, Journal of Geophysical Research, 101, 1295-1308, 1996b.

Fennel K., Wilkin, J., Levin, J. Moisan, J. O'Reilly, and D. Haidvogel, D.: Nitrogen cycling in the Middle Atlantic Bight: results from a three-dimensional model and implications for the North Atlantic nitrogen budget, Global Biogeochemical Cycles, 20, GB3007, 2006.

Ganju, N.K., Hayn, M., Chen, S.N., Howarth, R.W., Dickhudt, P.J., Aretxabaleta, A.L., Marino, R.: Tidal and groundwater fluxes to a shallow, microtidal estuary: constraining inputs through field observations and hydrodynamic modeling, Estuaries Coasts, 35, 1285-1298, 2012.

Ganju, N.K., Testa, J.M., Suttles, S.E., Aretxabaleta, A.L.: Spatiotemporal variability of light attenuation and net ecosystem metabolism in a back-barrier estuary, Biogeosciences Discussions: 10.5194/bg-2018-5335.

Ganju, N.K., and Kalra, T.S., Numerical model of Submerged Aquatic Vegetation (SAV) growth dynamics in West Falmouth Harbor: U.S. Geological Survey data release, https://doi.org/10.5066/P998IJGG, 2019.

Gallegos, C.L., Werdell, P.J., McClain, C.R., 2011.: Long-term changes in light scattering in Chesapeake Bay inferred from Secchi depth, light attenuation, and remote sensing measurements, Journal of Geophysical Research, 116, C00H08, 2011.

Gregg, W.W. and Carder, K.L.: A simple spectral solar irradiance model for cloudless maritime atmospheres, Limnology and. Oceanography, 35(8), 1657-1675, 1990.

Haidvogel, D.B., Arango, H.G., Hedstrom, K., Beckmann, A., Malanotte-Rizzoli, P., Shchepetkin, A.F. Model evaluation experiments in the North Atlantic Basin: simulations in nonlinear terrain-following coordinates. Dynamics of Atmosphere Oceans 2000, Vol. 32, pp. 239–281.

Haidvogel, D.B., Arango, H.G., Budgell, W.P., Cornuelle, B.D., Curchitser, E., Di Lorenzo E., Fennel, K., Geyer, W.R., Hermann, A.J., Lanerolle, L., Levin, McWilliams, J.C., Miller, Moore, A.M., Powell, T.M., Shchepetkin, A.F., Sherwood, C.R., Signell, R.P., Warner, J.C. and Wilkin, J.: Ocean forecasting in terrain-following coordinates: Formulation and skill assessment of the Regional Ocean Modeling System, Journal of Computational Physics, 227, 3595-3624, 2008.

Hamberg, J., Findlay, S.E.G., Limburg, K.E., Diemont, S.A.W.: Post-storm sediment burial and herbivory of Vallisneria americana in the Hudson River estuary: mechanisms of loss and implications for restoration: Storm burial and herbivory of Vallisneria, 25, 2017.

Hauxwell, J., Cebrian, J., and Valiela, I., Eelgrass Zostera marina loss in temperate estuaries: relationship to land-derived nitrogen loads and effect of light limitation imposed by algae, Vol.247:59-73, 2003.

Hayn, M., Howarth, R.W., Marino, M., Ganju, N., Berg, P., Foreman, K., Giblin, A, McGlathery, K.: Exchange of nitrogen and phosphorus between a shallow lagoon and coastal waters, Estuaries Coasts 37, S63-S73 (Suppl. 1), 2014.

Hemming, M.A., and Duarte, C.M.: Seagrass Ecology, Cambridge University Press, 2000.

Hipsey, M.R., and Hamilton, D.P.: Computational Aquatic Ecosystem Dynamic Model: CAEDYM v3 Science Manual. Centre for Water Research, 2008.

Jarvis, J.C., M.J. Brush, and K.A. Moore. 2014.Modeling loss and recovery of Zostera marina beds in the Chesapeake Bay: the role of seedlings and seed-bank viability. Aquatic Botany,113: 32-45.

Kalra, T.S.; Li, X.; Warner, J.C.; Geyer, W.R.; Wu, H. Comparison of Physical to Numerical Mixing with Different Tracer Advection Schemes in Estuarine Environments. Journal of Marine Science and Engineering, 2019, Vol. 7, 338.

Kalra, T.S., and Ganju. N. K., 2019, Idealized numerical model for Submerged Aquatic Vegetation (SAV) growth dynamics: U.S. Geological Survey data release, https://doi.org/10.5066/P973NL8J.

Kemp, W., Murray, L., Borum, J., and Sand-Jensen, K.: Diel growth in eelgrass *Zostera marina*, Marine Ecology Progress Series, 41, 79-86, 1987.

5   Kennish, M.J., Sakowicz, G.P. and Fertig, B.: Recent Trends of Zostera marina (Eelgrass) in a Highly Eutrophic Coastal Lagoon in the Mid-Atlantic Region (USA), Open Journal of Ecology, 6, 243-253, 2016.

Krause-Jensen, D., Middelboe, A.L., Sand-Jensen K, Christensen P.B.: Eelgrass, Zostera marina, growth along depth gradients: upper boundaries of the variation as a powerful predictive tool. Oikos, 91, 233-244, 2000.

Larkum, A. W., Orth, R. J., Duarte, C. M.: Seagrasses: Biology, Ecology and Conservation, Springer, 2006.

10 Liu, W.T., Katsaros, K.B., and Businger J.A.: Bulk parameterization of the air-sea exchange of heat and water vapor including the molecular constraints at the interface, Journal of Atmospheric Sciences, 36, 1722-1735, 1979.

Matsumoto, K., Tokos, K., Huston, A., and Joy-Warren, H.: MESMO 2: a mechanistic marine silica cycle and coupling to a simple terrestrial scheme, Geosci. Model Dev., 6, 477–494, https://doi.org/10.5194/gmd-6-477-2013, 2013.

Madden, C. J., Kemp, W. M..: Ecosystem Model of an Estuarine Submersed Plant Community: Calibration and Simulation of Eutrophication Responses: Estuarine Research Foundation, 19, No. 2B, 457-474, 1996.

15 McGlathery, K.J., Sundback, K., Anderson, I.C.: Eutrophication in shallow coastal bays and lagoons: the role of plants in the coastal filter, Marine Ecology Progress Series, 348, 1-18, 2007.

Moore, K.A.: Influence of Seagrasses on Water Quality in Shallow Regions of the Lower Chesapeake Bay, Journal of Coastal Research, 162-178, 2004.

20 Nixon, S.W., Buckley, B., Granger, S., Bintz, J.: Responses of very shallow marine ecosystems to nutrient enrichment, Human Ecological Risk Assessment: An International Journal, 7, 1457-1481, 2001.

Shchepetkin, A.F., and McWilliams, J.C. The Regional Ocean Modeling System: A split-explicit, free-surface, topography-following coordinates ocean model, Journal of Ocean Modelling 2005, Vol. 9, pp. 347–404.

Shchepetkin, A.F., McWilliams, J.C., Computational Kernel Algorithms for Fine-Scale, Multiprocess, Longtime Oceanic 25 Simulations, Handbook of Numerical Analysis 14, 121-183, 2009.

Sherwood, C.R., Aretxabaleta, A.L., Harris, C.K., Rinehimer, J.P., Verney, R., and Ferré, B., Cohesive and mixed sediment in the Regional Ocean Modeling System (ROMS v3.6) implemented in the Coupled Ocean–Atmosphere–Wave–Sediment Transport Modeling System (COAWST r1234), Geosci. Model Dev., 11, 1849–1871, https://doi.org/10.5194/gmd-11-1849-2018, 2018.

30 Sherwood, C.R., Signell, R.P., Warner, J.C., and Wilkin, J.: Ocean forecasting in terrain-following coordinates: formulation and assessment of the regional ocean modeling system, Journal of Computational Physics, 227, 3595-3624, 2008.

Short, F.T., and Neckles, H.A.: The Effects of Global Climate Change on Seagrasses, Aquatic Botany, 63, S0304-3770, 1999.

Smolarkiewicz, P.K. A fully multidimensional positive definite advection transport algorithm with small implicit diffusion. Journal of Computational Physics 1984, Vol. 54, pp. 325–362.

Terrados, J., Borum, J., Why are seagrasses important ? - Goods and services provided by seagrass meadows, 2006.

Thyng, K. M., Greene, C. A., Hetland, R. D., Zimmerle, H. M., & DiMarco, S. F.: True colors of oceanography.

5   Oceanography, 29(3), 10., 2016.

Warner J.C., Sherwood, C.R., Signell, R.P., Harris, C.K., and Arango, H.G.: Development of a three-dimensional, regional, coupled wave, current, and sediment-transport model, Computer & Geosciences, 34, 1284-1306, 2008.

Warner J. C., Armstrong, B., R. He, R., and Zambon, J.B.: Development of a Coupled Ocean-Atmosphere-Wave-Sediment Transport (COAWST) Modeling System, Ocean Modelling, 35, 230-244, 2010.

10   Woodward, P., and Colella, P., The numerical simulation of two-dimensional fluid flow with strong shocks. Vol.54(1), pp. 115-173, 1984.Zaldívar, J.M., F.S. Bacelar, S. Dueri, D. Marinov, P. Viaroli, and E. Hernández-García. 2009. Modeling approach to regime shifts of primary production in shallow coastal ecosystems. Ecological Modelling 220: 3100-3110.

Zharova, N, A. Sfriso, A. Voinov, B. Pavoni. 2001. A simulation model for the annual fluctuation of Zostera Marina biomass in the Venice lagoon. Aquatic Botany 70:135-150.

15   Zimmerman, R.C.: A biooptical model of irradiance distribution and photosynthesis in seagrass canopies, Limnology and Oceanography, 48, 568-585, 2003.

20

25

Model variables	Equivalent symbol in source code	Description of terms
α	AGB	Above ground biomass
β	BGB	Below ground biomass

γ	EPB	Epiphyte biomass
μ_s	ua_{SAV}	Maximum potential growth rate (SAV)
ρ_s	pp_{SAV}	Primary production (SAV)
φ_s	$llmt_{SAV}$	Light availability (SAV)
ϑ_s	$nlmt_{SAV}$	Nutrient limitation (SAV)
λ_s	$lambda_{SAV}$	Self-shading term (SAV)
δ_s	$agar_{SAV}$	Active respiration (SAV)
ε_s	$agbr_{SAV}$	Above ground basal respiration (SAV)
$\omega_{s,1}$	agm_{SAV}	Above ground biomass mortality (SAV)
$\omega_{s,2}$	bgm_{SAV}	Below ground biomass mortality (SAV)
θ	PAR	Photosynthetic Active Radiation (PAR)
$\sigma_{s,1}$	$agbg_{SAV}$	Translocation of above ground biomass to below ground biomass (SAV)
$\sigma_{s,2}$	$bgbg_{SAV}$	Translocation of below ground biomass to above ground biomass (SAV)
μ_e	ua_{EPB}	Maximum potential growth rate (EPB)
ρ_e	pp_{EPB}	Primary production (EPB)
φ_e	$llmt_{EPB}$	Light availability (EPB)
ϑ_e	$nlmt_{EPB}$	Nutrient limitation (EPB)
λ_e	$lambda_{EPB}$	Self-shading term (EPB)
$\varepsilon_{e,1}$	$aresp_{EPB}$	Active respiration (EPB)
$\varepsilon_{e,2}$	$bresp_{EPB}$	Basal respiration (EPB)
ω_e	$mort_{EPB}$	Mortality (EPB)
$\tau_{e,1}$	grz_{EPB}	Loss of EPB due to grazing
$\tau_{e,2}$	epb_{slgh}	Epiphyte biomass due to the SAV sloughing loss
t	$dtdays$	Time step in days

Table 1: SAV growth model variable descriptions

5

Input parameter	Equivalent symbol in model	Description	Default value	Units
g_s	scl	SAV growth fraction	0.03	None
r_s	arc	SAV active respiration coefficient	0.01	dtdays^{-1}
$T_{s,o}$	T_{OPT}	Optimum SAV growth temperature	15.0	°C
$\lambda_{s,max}$	$\lambda_{SAV,max}$	Self-shading parameter for SAV leaves (maximum AGB)	475.0	millimoles N m^{-2}
l_s	$klmt$	Half-saturation for light limitation for SAV	100.0	E m^{-2} s^{-1}
$n_{s,1}$	kn_t	Half-saturation for nutrient limitation for plant roots	100.0	millimoles
$n_{s,2}$	kn_{wc}	Half-saturation for nutrient limitation for plant leaves	5.71	millimoles
p_s	$arsc$	Maximum fraction of photosynthesis, SAV respiration	0.1	None
c_s	$bsrc$	Maximum fraction of SAV BGB biomass respired	0.0015	None
h_s	rc	SAV basal respiration coefficient (AGB and BGB)	0.069	dtdays^{-1}
m_α	km_{ag}	SAV AGB mortality rate (sloughing)	0.0005	dtdays^{-1}
m_β	km_{bg}	SAV BGB mortality rate	0.005	dtdays^{-1}
g_e	scl_{EPB}	Epiphyte growth fraction	0.2	None
r_e	arc_{EPB}	Epiphyte active respiration coefficient	0.0633	dtdays^{-1}
$T_{e,o}$	$T_{EPB,opt}$	Optimum growth temperature for epiphytes	25.0	°C
$\lambda_{e,max}$	$\lambda_{EPB,max}$	Self-shading parameter for epiphytes (maximum EPB)	475.0	millimoles N m^{-2}
l_e	kl_{EPB}	Half-saturation for light limitation for SAV	50.0	E m^{-2} s^{-1}
n_e	kn_{EPB}	Half-saturation for nutrient limitation for SAV	10.0	millimoles
p_e	$arsc_{EPB}$	Maximum fraction of photosynthesis, EPB active respiration	0.01	None
c_e	$brsc_{EPB}$	Maximum fraction of SAV BGB biomass respired	0.0015	None
h_e	rc_{EPB}	SAV basal respiration coefficient (AGB and BGB)	0.069	dtdays^{-1}
m_e	$kmort_{EPB}$	Mortality rate for epiphytes if no sloughing	0.001	dtdays^{-1}
$z_{e,max}$	$grz_{EPB,max}$	Maximum grazing rate on epiphytes	0.1	dtdays^{-1}
z_e	$grzk_{EPB}$	Grazing coefficient on epiphytes	0.01	None
k_1	kd_{trans}	Downward translocation coefficient	0.1	None
k_2	ku_{trans}	Upward translocation coefficient	0.02	None
m_f	mx_{frc}	Upward translocation coefficient	0.02	None

Table 2: SAV growth model input parameter descriptions and their values

5

Figure 1: Schematic showing the coupling of SAV growth module implementation in COAWST model.

Figure 2: Empirical relationships between above ground biomass and SAV shoot height for Z. marina populations in polyhaline regions of Chesapeake Bay and Chincoteague Bay. Data from Moore et al. 2004 and Ganju et al. 2018.
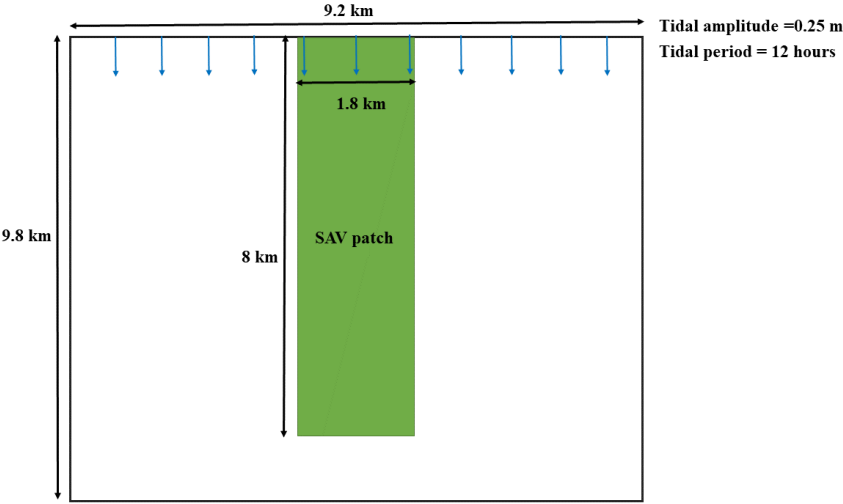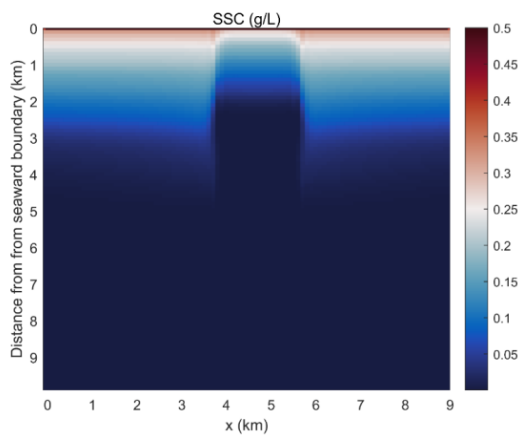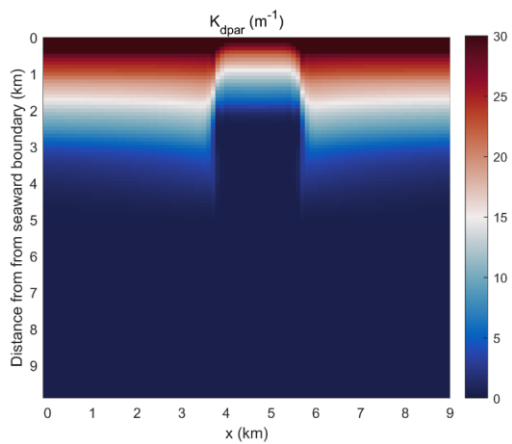
Figure 3: Planform view of the idealized test domain simulation.
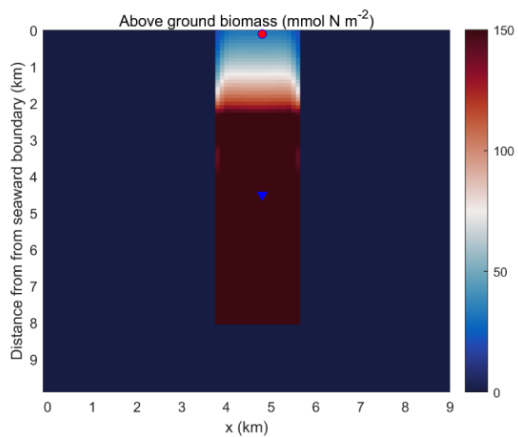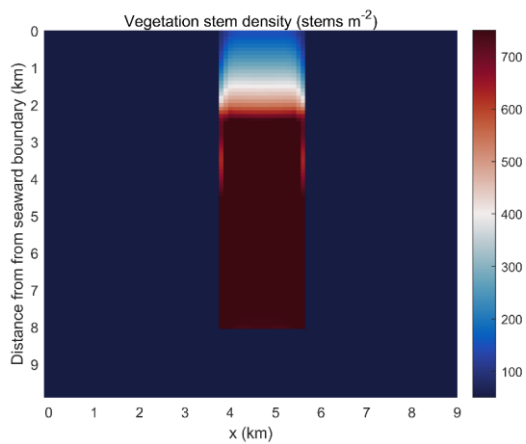
(a)

(b)

Figure 4: Planform view of (a) depth-integrated SSC, (b) light attenuation averaged over the last day of the simulation in the idealized domain.

(a)

(b)

Figure 5: Planform view of (a) above ground biomass and (b) vegetation stem density averaged over the last day of the simulation in the idealized domain. Red dot and blue triangle represent two points that are located at 0.1 km and 4.5 km into the SAV bed respectively.

(a)

(b)

(c)

(d)

Figure 6: Time-series of a) light attenuation, b) above ground biomass, c) net primary production of SAV ($\rho_s - \delta_s - \varepsilon_s$), and d) SSC in the bottom cell averaged every day from the two locations identified in Fig. 5a.

5

10

(a)

5

(b)

Figure 7. Magnitude of bottom stress (left) and depth-integrated SSC (right) at the end of the simulation plotted along the y axis of the idealized domain at two locations, including one outside (x=1.8 km; panel a) and one inside the SAV bed (x=4.8 km, panel b).

(a)   (b)

(c)   (d)

Figure 8. Mean over 22 days of a) depth-averaged chlorophyll, b) light attenuation, c) near-bottom PAR, and d) peak above ground biomass at day 14 of the simulation. Red circle indicated outer harbor (left) and blue triangle indicated inner harbor (right) points for time-series data in Figure 9.
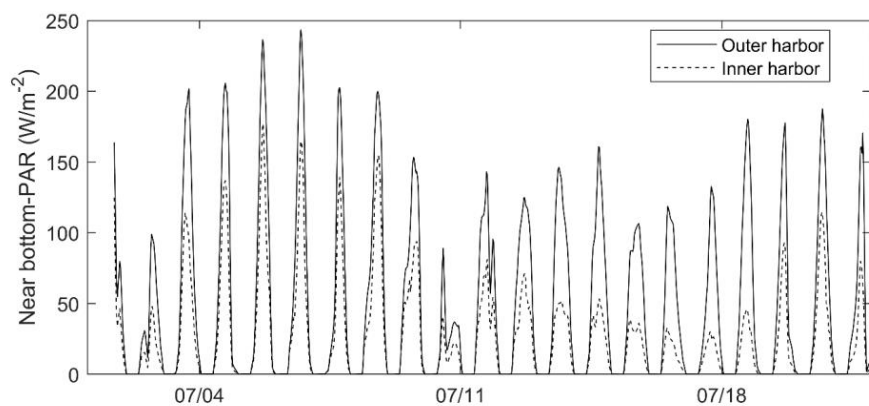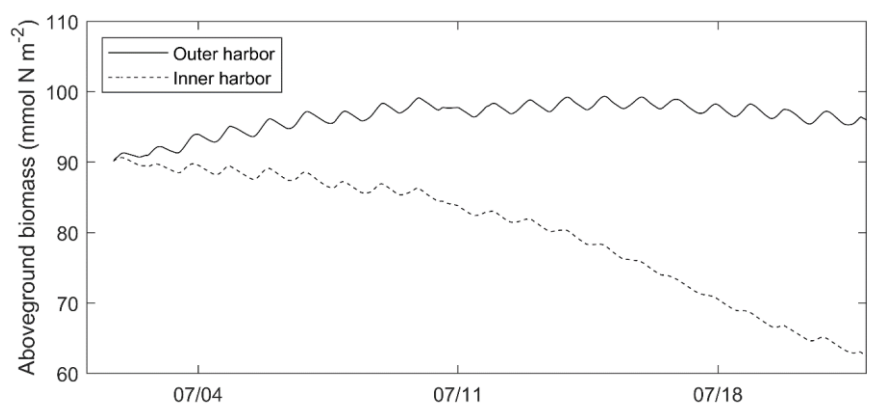
(a)

5

(b)

52

(c)

(d)

Figure 9. Time-series of a) chlorophyll, b) light attenuation, c) near-bottom PAR, and d) above ground biomass from outer and inner harbor locations identified in Figure 6.
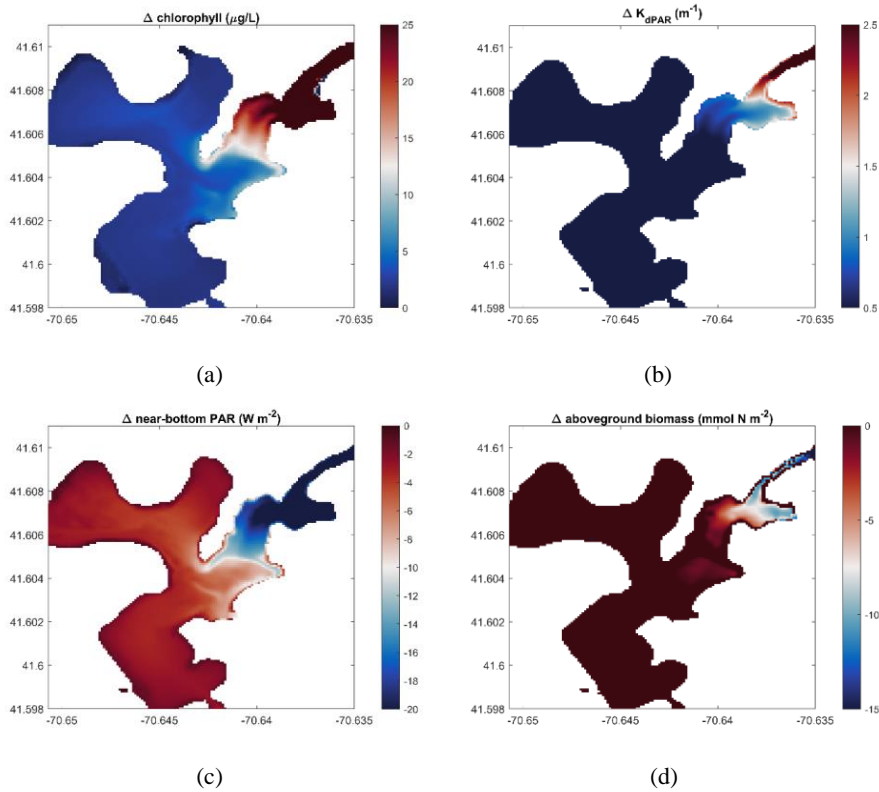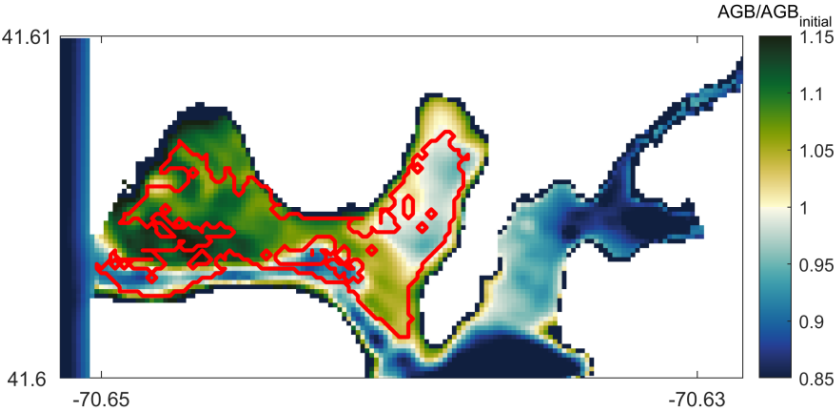
(a)

(b)

(c)

(d)

Figure 10. Change in outcomes between impacted and non-impacted scenario (nitrate loading scenario – no loading scenario). Difference in mean over 22 days of (a) depth-averaged chlorophyll, (b) light attenuation, (c) near-bottom PAR, and (d) peak above ground biomass at day 14 of the simulation.

Fig 11: Modeled AGB/AGB_{initial} (above ground biomass) distribution compared with field data showing seagrass coverage extent (red solid line). Values of AGB/AGB_{initial} > 1 represent seagrass growth potential and below 1 indicate potential seagrass decline at day 14 of the simulation.

5

10